Harnessing homeostatically active RhoC at cell junctions preserves human endothelial barrier function during inflammation

Natalia Colás-Algora[1], Pablo Muñoz-Pinillos[1], Susana Barroso[1], Cristina Cacho-Navas[1], Álvaro Caballero[1,2,3], Gema Cerro-Tello[1], Gema de Rivas[1], Martín González-Fernández[4], Ignacio Jiménez-Alfaro[5,6], Manuel Fresno[1], Catalina Ribas[1,2,3,7], Alberto Paradela[8], Eduardo López-Collazo[9,10], José Jesús Fernández[11] and Jaime Millán[1,*]

[1] Centro de Biología Molecular Severo Ochoa (CSIC-UAM), 28049, Madrid, Spain

[2] Departamento de Biología Molecular, Universidad Autónoma de Madrid, 28049 Madrid, Spain

[3] Instituto de Investigación Sanitaria La Princesa, 28006 Madrid, Spain

[4]Institute of Animal Pathology, Vetsuisse Faculty, University of Bern, 3012 Bern, Switzerland

[5] Departamento de Oftalmología, Fundación Jiménez Díaz, 28040 Madrid, Spain

[6] Instituto de Investigación Sanitaria, Fundación Jiménez Díaz, 28040 Madrid, Spain

[7] CIBER de Enfermedades Cardiovasculares, ISCIII (CIBERCV), 28029 Madrid, Spain

[8]Centro Nacional de Biotecnología (CSIC), 28049, Madrid, Spain

[9]The Innate Immune Response Group, IdiPAZ, Hospital Universitario La Paz, 28046, Madrid, Spain

[10]CIBER of Respiratory Diseases (CIBERES), Madrid, Spain.

[11] Centro de Investigación en Nanomateriales y Nanotecnología (CINN-CSIC). Instituto de Investigación Sanitaria Principado de Asturias (ISPA), 33940, Oviedo, Spain

Running title: RhoA subfamily activation protects from systemic inflammation

[*]Correspondence: Jaime Millán, Centro de Biología Molecular Severo Ochoa. Universidad Autónoma de Madrid, Cantoblanco, 28049, Madrid, Spain.

Phone: 0034911964713

email: jmillan@cbm.csic.es

Keywords: cytotoxic necrotizing factor, RhoA, RhoB, RhoC, endothelial barrier function, VE-cadherin, PECAM-1, reticular adherens junction, LPS, edema, sepsis, actin, myosin II, quantitative proteomics.

Number of characters: 90475

Number of Figures: 8

Number of Supplemental Figures: 10

SUMMARY

The GTPase RhoA plays a critical role in generating actomyosin-mediated contractile forces that cause endothelial hyperpermeability during systemic inflammatory diseases. RhoA is almost identical to RhoB and RhoC, all of which are molecular targets of specific bacterial toxins. Searching for new treatments to modulate Rho-dependent endothelial integrity, we demonstrate that the selective and simultaneous activation of these three Rho GTPases with a chimeric recombinant toxin does not induce cell contraction but enhances microvascular endothelial barrier function in response to pathological inflammatory challenges *in vitro* and *in vivo*. This pro-barrier effect is specifically mediated by RhoC, whose activity is increased by cell confluence. The uniqueness of RhoC relies on an arginine residue (R188) within its hypervariable region that determines its junctional localization, high homeostatic activity, and barrier-protective function, in contrast to the permeability-inducing, low homeostatic activity of RhoA and RhoB. Quantitative proteomics and high-resolution confocal microscopy revealed that RhoC regulates perijunctional actomyosin and the expression of myosin light chain proteins. Thus, harnessing the activity of RhoC represents a potential therapy for strengthening endothelial barriers during pathological inflammation.

INTRODUCTION

Systemic and exacerbated inflammatory responses, such as those caused by infection or trauma in sepsis, leads to life-threatening organ edema and dysfunction. The uncontrolled secretion of inflammatory mediators in these pathologies generates a cytokine storm that enters the circulation and alters endothelial permeability, increasing vascular leakage even if the causes giving rise to the damaging inflammatory response are successfully identified and treated (Goldenberg et al., 2011; Fajgenbaum and June, 2020). Current strategies for preventing fatal tissue edema during sepsis are focused on inhibiting this inflammatory signaling and stabilizing the vascular tone (Fajgenbaum and June, 2020; Rittirsch et al., 2008; Colás-Algora et al., 2023). However, given the importance of the vasculature in this pathology (Teuwen et al., 2020; Goldenberg et al., 2011), a complementary strategy, which has yet to be thoroughly explored, may consist of transiently reinforcing the endothelium during the critical illness period, regardless of the specific mediators responsible for vascular leakage.

Endothelial barrier integrity is regulated by the family of Rho GTPases, molecular switches that control multiple functions, including the actin cytoskeleton, a major endothelial scaffold. In the current paradigm of molecular pathways governing endothelial barrier function, RhoA, the founder member of this family, is the central regulator of stress fiber formation and F-actin-mediated contraction, which compromise the endothelial integrity in response to acute inflammatory signals such as thrombin or histamine both *in vivo* and *in vitro* (Mikelis et al., 2015; Amerongen et al., 2000). This GTPase acts in opposition to the GTPase Rac1, which mediate endothelial barrier enhancement (Beckers et al., 2010; Garcia et al., 2001; Komarova et al., 2007; Marcos-Ramiro et al., 2016; Timmerman et al., 2015; van Nieuw Amerongen et al., 1998).

RhoA belongs to a subfamily that comprises another two GTPases, RhoB and RhoC, which share 88% amino acid identity (Lawson and Ridley, 2018; Wheeler and Ridley, 2004). They regulate common effectors, such as Rho kinases (ROCK) and play redundant, complementary and specific roles depending on the cellular context (Marcos-Ramiro et al., 2016; Vega et al., 2011; Wheeler and Ridley, 2004). The main sequence divergence between RhoA, RhoB, and RhoC is localized in the C-terminal hypervariable region, which is essential for their prenylation and membrane localization (Ridley, 2013).

Vascular endothelial (VE)-cadherin-dependent adherens junctions (AJs) are the main regulators of endothelial barrier integrity (Dejana, 2004). VE-cadherin partners with cytoplasmic catenins, which connect AJs to the underlying actin cytoskeleton that stabilizes this junctional protein complex. VE-cadherin cross talks with other junctional protein complexes, such as those formed by PECAM-1, into distinct junctional structures with reticular morphology that stabilize contacts between cells (Fernandez-Martin et al., 2012; Klomp et al., 2019). PECAM-1 and VE-cadherin also form a mechanosignaling module (Tzima et al., 2005) that signals to actin stress fibers through Rho GTPases. Surface VE-cadherin also participates in cell survival, collective endothelial cell migration and gene transcription (Carmeliet et al., 1999; Dejana, 2004; Giannotta et al., 2013; Hayer et al., 2016) so its expression is closely regulated even when endothelial barrier integrity is transiently disrupted by inflammatory mediators (Colas-Algora et al., 2019).

We had previously reported that RhoB has a specific function as a negative regulator of barrier function in an inflammatory context in endothelial cells (Marcos-Ramiro et al., 2016) and, as had other laboratories, that inhibiting the RhoA subfamily effector ROCK prevents acute contraction induced by inflammatory mediators junctions

(Fernandez-Martin et al., 2012; Vandenbroucke et al., 2008; van Nieuw Amerongen et al., 2000). Here, unexpectedly, we found that activating endogenous RhoA, RhoB and RhoC with a chimeric protein containing the catalytic domain of the cytotoxic necrotizing factor y (CNFy) toxin from *Yersinia pseudotuberculosis*, far from inducing contraction, increases reticular AJs and perijunctional F-actin, maintains endothelial barrier function *in vitro*, prevents local microvascular disruption in response to inflammatory mediators *in vivo*, and reduces organ edema upon systemic LPS stimulation. Hence, this RhoA activator emerges as a potential therapeutic approach for pathologies associated with endothelial barrier dysfunction. More importantly, it has led us to demonstrate that, despite its similarity to RhoA and RhoB, RhoC plays an opposite, barrier-protective role that mediates the effect of this chimeric protein. One single, positively charged, C-terminal R188 residue in RhoC, which is not present in the equivalent position of RhoA or RhoB, determines the localization, high activity and pro-barrier function of this GTPase. Hence, the spatiotemporal control of the RhoA GTPase subfamily activity and the relative expression of each of its members determine its pro-barrier or anti-barrier roles, which could be therapeutically exploited.

RESULTS

Activation and inhibition of endogenous RhoA, RhoB and RhoC show that their GTPase activity is necessary for maintaining endothelial barrier function and reticular AJs.

Cytotoxic necrotizing factors (CNFs) are bacterial toxins that induce deamidation of a glutamine residue in the Switch II region of Rho GTPases, blocking their GTPase activity and thus constitutively activating these enzymes. Some CNFs, such as CNF1, induce deamidation of various Rho GTPases, such as those from the Rac, RhoA and Cdc42 subfamilies. Some others, such as CNFy, are specific to the RhoA subfamily (Aktories, 2015; Schlegel et al., 2011; Schmidt et al., 1997). We had previously reported an essential role of RhoA and RhoB decreasing human endothelial barrier function in an inflammatory context (Marcos-Ramiro et al., 2016; Fernandez-Martin et al., 2012). To investigate further the role of the RhoA subfamily of GTPases in human endothelial cells, we used CN03, a commercially available recombinant protein that contains the catalytic domain of a CNF toxin and that is conjugated to a cell-penetrating peptide that translocates the toxin into the cell after 2-3 hours of exposure (Ortega et al., 2016). CN03 activated RhoA, RhoB and RhoC but not Cdc42 or Rac1 in primary human vascular endothelial cells (Figures 1A and S1A) confirming our previous analyses in other cell types (Ortega et al., 2016). Interestingly, CN03 promoted the formation of robust VE-cadherin-mediated AJs with a reticular morphology in various endothelial beds such as HUVECs (Figure 1B, boxed areas) and HDMVECs (Figure 1C, boxed areas). Reticular AJs are cell-cell contact domains where VE-cadherin crosstalk with the junctional adhesion receptor PECAM-1 (Fernandez-Martin et al., 2012). The reticular architecture of VE-cadherin and PECAM-1 reduces endothelial permeability, has been found *in vivo* and *in vitro* (Reglero-Real et al., 2021; Klomp et al., 2019; Fernandez-Martin et al., 2012; Colás-Algora et al., 2023) and is disrupted by inflammatory cytokines, anti-PECAM-1 blocking antibodies and autophagy (Fernandez-Martin et al., 2012; Reglero-Real et al., 2021). Indeed, VE-cadherin and PECAM-1 staining intensities at cell–cell contacts, as well as areas covered by reticular AJs, were notably higher in cells exposed to CN03 (Figures 1B and 1C), which was linked to an increase of total and surface protein levels of these two junctional proteins (Figures 1D-F). Together, these experiments indicate that CN03 activates RhoA, RhoB and RhoC, but far from inducing cell contraction and disrupting cell-cell contacts, this chimeric protein strengthens endothelial AJs (Figure 1F).

To analyze endothelial barrier properties in a complementary and quantitative manner, we measured multifrequency transendothelial resistance (TEER) of primary human endothelial cells exposed or not to CN03, using an ECIS system. CN03 increased TEER, which confirmed that this RhoA subfamily activator reinforces endothelial barrier integrity (Figure 1G). Moreover, ECIS can mathematically model multifrequency TEER measurements and separate it into three parameters of different biological meanings: Rb, which provides the contribution of paracellular permeability and cell-cell junctions to barrier integrity; α, which measures cell-matrix interactions; and Cm, which is relative to the membrane capacitance (Tiruppathi et al., 1992; DePaola et al., 2001; Colás-Algora et al., 2020). The significant increase of TEER observed in cells treated with CN03 was mostly caused by changes in Rb values, but not in α or Cm, indicating that this recombinant protein exerts a protective effect related with junction-related paracellular permeability (Figure S1B). Finally, to identify the exact nature of CN03 we performed mass spectrometry analysis of its peptide sequence, which revealed that it is a chimeric toxin containing the N-terminal domain of CNF1 from *Escherichia coli* and the C-term catalytic domain of CNFy from *Yersinia pseudotuberculosis,* which specifically activates RhoA proteins (Figure S1C). This fusion protein is very similar to that previously reported by Hoffman et al. (Hoffmann et al., 2007).

To address the role of the RhoA subfamily activity using an alternative strategy, we analyzed the effect of inhibiting these three GTPases with C3 transferase, an exoenzyme from *Clostridium botulinum* (Aktories and Hall, 1989; Marcos-Ramiro et al., 2016). C3 transferase did not significantly change the TEER values. However, multifrequency TEER modeling revealed a massive decrease in Rb, concomitant with an increase in α and Cm, indicating that, despite not altering the TEER values, C3 induces a substantial increase in paracellular permeability that is compensated by an increase in adhesion to the substratum and changes in the membrane capacitance (Figure S2A). Consistent with these results, confocal microscopy analyses revealed that C3, which massively reduced F-actin staining, induced many intercellular gaps in confluent cells (Figure S2B, arrowheads). Overall, the use of different recombinant proteins with capacity to modulate the activity of endogenous RhoA, RhoB and RhoC, indicate that the activity of the RhoA subfamily is necessary for maintaining the barrier properties of primary human endothelial cells.

The CN03-induced reticular architecture preferentially stabilizes junctional VE-cadherin

To investigate further the effect of CN03 on VE-cadherin-mediated AJs, we generated a construct to express a photoconvertible VE-cadherin-Dendra2 chimera in endothelial cells. Confluent cells were exposed or not to CN03 for 3 h before photoconversion of VE-cadherin-Dendra2 at cell-cell junctions (Figure 2A). VE-cadherin at reticular AJs exhibited lower diffusion rate than when this adhesion molecule was distributed with linear morphology, indicating that the reticular disposition favors the stability of junctional protein complexes. In fact, CN03 not only increased reticular AJs, but also reduced dispersion of VE-cadherin in both linear and reticular AJs (Figures 2B and 2C). We explored in greater depth the structure of reticular AJs and the reason why this disposition strengthens endothelial barrier integrity. By expressing PECAM-1-GFP we localized reticular areas for analysis by transmission electron microscopy (EM) (not shown). We then acquired EM micrographs of serial sections and performed a 3D reconstruction. The 3D analyses revealed superimposed plasma membranes between adjacent cells in which their interface was irregular and featured invaginations that suggested active processes of internalization and intercellular communication (Figure 2D, arrowheads). These results indicate that reticular AJs provide an extra source of plasma membrane that increases the surface area in which to form intercellular protein complexes. The extension of these cellular interfaces potentially copes with changes in vessel diameter and cellular shape caused by the mechanical stress induced by inflammation, blood pressure, trauma, etc., thereby helping maintain the integrity of the endothelial monolayer.

CN03 ameliorates endothelial barrier disruption *in vitro,* and local and systemic vascular leakage *in vivo,* in response to an inflammatory challenge.

We then analyzed the effect of CN03 when endothelial cells are previously exposed to an inflammatory challenge that induces pathological hyperpermeability. In response to LPS, CN03 significantly attenuated the reduction of TEER and Rb values in HDMVECs, both of which recovered to levels close to those before to the exposure to the inflammatory challenge (Figure 3A). The LPS-induced dispersion of VE-cadherin and PECAM-1 from junctions, along with the formation of intercellular gaps, also significantly decreased (Figure 3B). During sepsis, circulating blood with high levels of inflammatory mediators induces microvascular leakage and edema. The lung is one of the main organs affected by microvascular hyperpermeability. To mimic this systemic pathology in human cells, we analyzed the effect of two sets of sera collected from healthy donors and severely ill patients with sepsis on lung microvascular endothelial cell barriers (HLMVECs), as previously described (Colás-Algora et al., 2023). Septic sera induced a stronger disruption of HLMVEC barrier than sera from healthy donors (Figure 3C). Interestingly, septic sera also induced cell contraction and the appearance of massive intercellular gaps that were significantly reduced by CN03 (Figures 3D and 3E). Hence, overall, reinforcing the human endothelium with CN03, strongly protects these cellular barriers from pathological proinflammatory challenges.

We then tested the effect of intravenous injection of CN03 in a mouse model of local induction of vascular leakage. Intravenous injection of Evans blue was followed by injection of LPS, VEGF and control saline buffer into the skin (Figure 4A). CN03 pretreatment significantly reduced vascular leakage by almost 50% in LPS-injected skin patches, and had a milder effect on VEGF-induced vascular leakage. In contrast, measurements of Evans blue revealed that CN03 did not affect homeostatic vascular leakage in liver, lung or kidney (Figure S3A). Systemic bacterial, viral or fungal infection causes a cytokine storm that triggers endothelial barrier disruption, organ edema and failure during sepsis (Goldenberg et al., 2011). To evaluate the effect of CN03 systemically *in vivo*, the acute phase of bacterial sepsis was mimicked by intraperitoneal injection of LPS in the presence of saline or CN03. CN03 significantly reduced the increase of TNF and IL-6 concentration in blood (Figure 4B) and systemic vascular leakiness measured by Miles assay in livers, lungs and kidneys (Figure 4C) (Miles and Miles, 1952). In contrast, CN03 had no significant effect on LPS-induced hypoglycemia (Figure S3B). Therefore, our results clearly show that the activation of endogenous RhoA subfamily proteins by CN03 reduces blood inflammatory cytokines, endothelial barrier disruption and vascular leakage when systemic inflammation is induced.

The effect of CN03 on endothelial barrier function is dependent on RhoC expression

To gain insight into the contribution of each RhoA subfamily member to the effect of CN03 on endothelial barrier function, we compared the morphological changes induced by this chimeric protein on cell-cell junctions of endothelial cells silenced, or not, for each of the three *RHOA* subfamily genes. First, single *RHO* gene knockdown had a significant effect on the expression of the other family members. As previously reported (Marcos-Ramiro et al., 2016), single silencing upregulated the expression of at least another RhoA-subfamily protein in HUVECs (Figure 5A) and in HDMVECs (Figure S4A). Such upregulation also involved an increase in the activity of the corresponding Rho protein, except for RhoB, which remained mostly inactive (Figure S4B). These compensations suggest that the individual members of the RhoA subfamily of GTPases play additive and redundant roles in human endothelial cells. In contrast, single or double knockdown of these three GTPases did not significantly affect the expression or activity of other distant members of the Rho family, such as Rac1 or Cdc42 (Figure S4C). TEER and Rb analyses of single RHO gene silencing indicated that RhoA expression reduces endothelial barrier integrity, whereas RhoC expression is necessary for maintaining barrier function (Figure 5B). No major changes were detected in other parameters related with endothelial barrier function (Figure S4D). In contrast with previous reports suggesting a significant role for RhoB in endothelial permeability (Pronk et al., 2019), we observed no major effect on permeability when RhoB expression was reduced in HUVECs. These findings are consistent with previous data showing low levels of RhoB expression in HUVECs that had not been exposed to inflammatory mediators for several hours (Marcos-Ramiro et al., 2016) and is also in accordance with the low levels of activation detected for this GTPase (Figure S4B). In contrast, similar to RhoA, single depletion of RhoB reinforced the endothelial barrier in HDMVECs, whereas RhoC silencing once more resulted in reduced TEER and, notably, Rb, thereby demonstrating the specific role of RhoC expression in maintaining paracellular permeability also in the human microvascular endothelium (Figure S4E). Moreover, RhoA and RhoB knockdown did not affect the CN03-dependent increase of VE-cadherin and PECAM-1 at the cell periphery, whereas RhoC knockdown significantly disrupted the formation of cell-cell junctions (Figures 5C and 5D). Cells lacking RhoC also failed to localize VE-cadherin and PECAM-1 to cell-cell contacts upon exposure to CN03, despite being initially seeded at high density to promote confluence (Figures 5C and 5D). Furthermore, *RHOC* gene silencing not only dispersed VE-cadherin and PECAM-1 but also markedly reduced the expression of the former, as revealed by western blot analyses of cells transfected for four different siRNA oligonucleotides (Figure S5A). qPCR assays indicated that this reduction was not transcriptional (Figure S5B), but was related to protein stability, as RhoC knockdown reduced VE-cadherin half-life (Figure S5C). Finally, the three RhoA subfamily members were individually or simultaneously silenced, and the expression analyses were extended to additional components of cell-cell junctions. Although RhoA and RhoB moderately regulated the expression of some junctional proteins, and triple Rho silencing reduced the expression of other endothelial cadherins such as N-cadherin (Figures S5D and S5E) (Colas-Algora and Millan, 2019), the presence of RhoC was mostly necessary to maintain the expression of VE-cadherin and α-catenin. Collectively, these findings demonstrated that RhoC is the sole member of the subfamily that strengthens endothelial barrier function. Such enhancement occurs specifically through the stabilization of VE-cadherin-mediated AJs.

To investigate the differences among the three members of the RhoA subfamily in greater detail, we analyzed the barrier properties of cells manipulated so that they predominantly expressed only one of these GTPase. Similar to single RhoA subfamily depletion, simultaneous depletion of two GTPases induced an almost three-fold upregulation of the remaining Rho, resulting in an overall enrichment of five- to ten-fold with respect to the silenced GTPases in HUVECs (Figure 5E) and in HDMVECs (Figure S6). The double-depleted cells were thus termed “only RhoA”, “only RhoB” and “only RhoC”. Only RhoC cells did not alter the junctional recruitment of VE-cadherin (Figure 5F) but did remarkably increased PECAM-1 expression (Figure 5E) and junctional localization, and displayed abundant reticular, PECAM-1-enriched AJs (Figure 5F), consistent with previous reports that attributed this particular junctional morphology to this adhesion receptor (Fernandez-Martin et al., 2012). Although only

RhoA and only RhoC cells were able to maintain homeostatic barrier function, only RhoB cells showed reduced TEER and Rb values, indicating that the upregulation of this Rho GTPases cannot fully compensate the lack of the other two, probably due to its partial and specific endosomal localization (Figure S7A). Moreover, only RhoA and only RhoB cells could not reinforce AJs in response to the CN03 treatment, in addition to a moderate increase in Rb values observed in homeostatic conditions (Figures S7B and S7C). Finally, only RhoC cells displayed reduced barrier hyperpermeability and increased the protective effect of CN03 from 6 h onwards after LPS stimulation (Figures 5G and S7D). Together, these experiments demonstrate that the RhoA subfamily is essential for regulating paracellular permeability, but that its pro- or anti-barrier function in the human endothelium depends on the relative expression of individual members of the family. Endothelial cell barriers that mostly express RhoC are more resistant to inflammatory disruptors.

Quantitative proteomics and confocal microscopy reveal that RhoC regulates the expression of VE-cadherin by controlling perijunctional actomyosin through MLCK

To better understand the molecular mechanisms underlying the specific role of RhoC in maintaining cell-cell contacts and VE-cadherin protein stability, we performed label-free differential proteomics analyses between cells transfected with siRNA control and cells silenced for RhoC with two different siRNA oligonucleotides. In addition to detecting lower levels of some proteins forming AJs, already observed in the junctional protein screening (Figure S5E), such as α-catenin (Table S1), quantitative proteomics revealed significant alterations in the expression of non-muscle myosin-II components (Figures 6A-C). Non-muscle myosin II is an actin-based molecular motor forming a hetero-multimeric protein complex comprising homodimers of motor myosin heavy chains (MHCs) associated with two sets of pairs of myosin light chains (MLCs): regulatory and essential. The regulatory MLCs control ATP-dependent conformational changes in MHCs, which mediate contraction by sliding actomyosin filaments alongside each other in an antiparallel way (Heissler and Manstein, 2013; Agarwal and Zaidel-Bar, 2019). In addition, MLCK and Rho Kinase (ROCK) regulate myosin-II-mediated contraction by phosphorylating these regulatory MLCs. Quantitative proteomics revealed a consistent decrease of proteins related to myosin-II activity in RhoC depleted cells, such as the regulatory MLCs, MYL9 and MYL12B, and the essential MLCs, MYL6 and MYL6B (Figure 6B) (Table S1) (Park et al., 2011). Western blot against MLC-2 (MYL9) and phospho-(S-19) MLC (MYL9 and MYL12B) (Oya et al., 2021) confirmed these changes and revealed that each of the three RhoA subfamily members contribute to the expression and phosphorylation of MLC, although RhoC silencing caused the strongest reduction (Figure 6C). However, this additive effect on regulatory MLC did not explain de contrary effects of RhoA and RhoC on barrier function. We hypothesized that each member of this subfamily can regulate these motor proteins in different regions of the human endothelial cell and then analyzed the effect of single Rho depletion on actomyosin by confocal microscopy. The lack of RhoC sharply reduced F-actin levels and preferentially decreased peripheral actin fibers (Figures 6D and 6E). RhoB knockdown, which increases RhoA and RhoC expression levels but had no effect on barrier function, induced an overall increase in F-actin, whereas RhoA silencing did not promote a significant actomyosin reorganization (Figures 6D and 6E). Interestingly, the immunostaining of phosphorylated MLC in homeostatic conditions was preferentially localized at the periphery of the cell, from where it relocated to central stress fibers mostly upon RhoC knockdown, but not when

RhoA and RhoB were depleted, although knocking down RhoB promoted a significant dispersion of p-MLC (Figure 6D). In agreement with a RhoC-dependant regulation of peripheral actomyosin, only RhoC cells (Figure 6F) and cells exposed to CN03 (Figure 6G) exhibited robust perijunctional F-actin, confirming that modulating Rho expression with siRNA, or Rho activity with CN03, promotes changes in the spatiotemporal localization of F-actin polymerization.

It has been shown that MLC activation and phosphorylation can be mediated by the Rho kinase (ROCK), which phosphorylates MLC at the cell center, and the myosin light-chain kinase (MLCK), which localizes in cortical actin bundles and regulates MLC phosphorylation at cell borders (Totsukawa et al., 2000). To test whether myosin-II activation and VE-cadherin expression levels are mechanistically coupled, we analyzed the effect of the ROCK inhibitor Y27632 and the MLCK inhibitor ML-7 on MLC phosphorylation, VE-cadherin levels and barrier function. Y27632 clearly reduced MLC phosphorylation, but had no major effect on VE-cadherin levels, consistent with findings in previous analyses (Fernandez-Martin et al., 2012; Marcos-Ramiro et al., 2014). In contrast, although the effect of the MLCK inhibitor ML-7 on MLC phosphorylation was not as strong as that of Y27632, it clearly decreased the levels of VE-cadherin protein expression and endothelial barrier function (Figures S8A and S8B). Accordingly, ML-7, but not Y27632, generated intercellular gaps (Figure S8C, arrowheads). Together, these experiments indicate that MLCK and the RhoC-mediated control of peripheral actomyosin regulate VE-cadherin expression and endothelial barrier function.

RhoC is the only RhoA subfamily member that is homeostatically active and localized at cell borders

We investigated why CN03 has a net barrier-enforcing effect despite it similarly activates anti-barrier RhoA and RhoB and pro-barrier RhoC. We and other researchers had previously shown that unstimulated primary human endothelial cells express equal levels of RhoA and RhoC mRNA (Reinhard et al., 2016) and protein (Marcos-Ramiro et al., 2016) but reduced levels of RhoB, whose expression is only increased upon long-term cytokine stimulation (Marcos-Ramiro et al., 2016). We quantified the relative levels of activation of these three proteins by analyzing the ratio between the GTP-loaded Rho proteins, isolated by pulldown assays, and Rho protein expression detected in the initial cell lysates. We found that RhoC is almost eight times more active than RhoA and four times more active than RhoB (Figure 7A). Since RhoB expression levels are very low relative to those of RhoA and RhoC in quiescent endothelial cells (Marcos-Ramiro et al., 2016), these results show that RhoC accounts for most of the active RhoA subfamily proteins in unstimulated confluent human endothelial cells. In addition, only RhoC was found to be associated with the plasma membrane in surface protein biotinylation assays that enabled the fractionation of proteins exposed to the extracellular milieu along with proteins associated with them (Figure 7B). Furthermore, while active, GTP-bound Rho GTPases are typically translocated to the plasma membrane, their GDP-bound, inactive forms complex with RhoGDI proteins in the cytoplasm, masking the Rho prenylated hypervariable region responsible for membrane translocation. Immunoprecipitation with antibodies against Rho proteins revealed that RhoA was more strongly associated with RhoGDI compared with RhoC, in accordance with the prevalent activation of RhoC with respect to RhoA in confluent human endothelial barriers (Figure 7C). It is of note that, RhoC also coprecipitated with RhoA, as recently described in the proximity interaction network of Rho GTPases (Bagci et al., 2020), but not inversely. Finally, similar to the analyses previously performed in primary human vascular endothelial cells (Marcos-Ramiro et al., 2016) and human corneal endothelial cells (Santander-García et al., 2016), we quantified the relative expression levels of endogenous RhoA, RhoB, and RhoC proteins in murine microvascular endothelial cells isolated from lungs. We found that RhoC is predominantly expressed compared to RhoA and RhoB, suggesting that this GTPase is central to microvascular endothelial cell function in murine experimental models as well (Figure 7D). Collectively, these results demonstrate the dominant role of RhoC with respect to its closest GTPases, particularly RhoA, which remains mostly inactive in homeostatic conditions. Since CN03 similarly activates RhoA, RhoB, and RhoC in human endothelial cells (Figure 1A), the absolute number of activated RhoC molecules is far greater than those of activated RhoA and RhoB, tipping the balance of CN03 effect toward strengthening the endothelial barrier.

Interestingly, cell confluency significantly increased the expression and activation of RhoC, but not of RhoA, suggesting that homeostatically active RhoC is regulated by endothelial cell-cell junctions (Figure 7E). Confocal analyses with specific antibodies revealed that RhoC was evenly distributed throughout the cell, but becoming more concentrated at cell borders in response to CN03 (Figure 7F, enlarged area). Junctional RhoC was also observed in only RhoC cells, whereas RhoA staining was not confined to any cellular structure in siControl and only RhoA cells. RhoB distribution was mostly in endosomes in siControl and only RhoB cells (Figure S9A), as previously described (Marcos-Ramiro et al., 2016). We further examined the effect of CN03 on the localization of RhoC activity by carrying out a FRET analysis with the RhoC FLARE biosensor, which consists of the Rho binding domain of ROCK (RBD) (residues 905-1046), conjugated with full-length RhoC and flanked by monomeric fluorescent proteins able to undergo FRET when RBD binds activated RhoC (Figure S9B) (Zawistowski et al., 2013). As a prior control, we observed higher FRET in RhoC constitutively active (Q63L) FLARE and a lower FRET in RhoC dominant negative (T19N) FLARE, than in RhoC FLARE (Figure S9C). FRET between the two fluorophores was preferentially detected close to the border of endothelial cells expressing RhoC FLARE (Figure 7G). Moreover, CN03 selectively increased FRET signal at the cell periphery, consistent with the translocation observed for endogenous RhoC, and indicating that this chimeric protein promotes RhoC activation at cell borders.

The junctional localization and high activity of RhoC depend on the R188 residue from the hypervariable region

Collectively, or results show that the activity of RhoC is significantly higher than that of RhoA and RhoB (the level of RhoB expression is comparatively very low in HUVECs), specifically depends on cell confluency and occurs close to cell-cell junctions, probably due to the concentration of various Rho GEFs in these domains (Mahlandt et al., 2023; Holzner et al., 2021; Khan et al., 2021). We investigated the molecular basis of such contrasting differences between RhoC and RhoA. The C-terminal hypervariable regions of these two GTPases are their most divergent protein domains and contain the prenylation site that enables their lipid modifications and localization to the plasma membrane upon activation. RhoA and RhoC have polybasic sequences adjacent to their prenylation C residue, but RhoA also contains a phosphorylatable S residue that is absent from RhoC (Lang et al., 1996). First, we conjugated these hypervariable regions to the C-terminus of GFP (GFP-RhoA-hyper and GFP-RhoC-hyper) to determine whether they are sufficient to target this fluorescent protein to VE-cadherin-positive membrane domains (Figure 8A). GFP-RhoC-hyper partially colocalized with VE-cadherin to a greater extent than GFP-RhoA-hyper. As expected, when the prenylation C-residue was mutated to G (GFP-RhoA/C-hyper^{C190G}), the two chimeric GFP constructs became mostly cytoplasmic. Substituting the R188 residue of RhoC by an S, as occurs in the hypervariable region of RhoA (GFP-RhoC-hyper^{R188S}), reduced the junctional localization of the fluorescent chimera. Reciprocally, substituting the S188 residue of the RhoA segment by an R, as in the RhoC hypervariable domain, (GFP-RhoA-hyper^{S188R}), increased junctional staining, indicating that this position is fundamental for Rho localization. Mutating these residues in the full GFP-RhoC proteins had a similar effect in the junctional localization of the protein (Figure 8B) This outcome was not specific to the S substitution, since GFP-RhoC^{R188A} displayed a reduction in junctional localization with respect to GFP-RhoC similar to that of GFP-RhoC^{R188S}, suggesting that the positive charge of R188 residue is fundamental to targeting RhoC to the membrane. Importantly, the alterations in membrane localization of these mutants were associated with changes in RhoC activity (Figure 8C). Moreover, overexpression of the GFP-RhoC, but not of the GFP-RhoA or GFP-RhoC^{R188S}, reinforced endothelial barrier function (Figures 8D and S10A), revealing the pivotal role of R188 in the specific pro-barrier effect of RhoC. It is of note that the reciprocal mutation in GFP-RhoA, GFP-RhoA^{S188R}, increased its junctional localization but did not increase its activity indicating that other molecular features intervene in the regulation of this GTPase (Figures S10B and S10C). Thus, the R188 residue contributes to the functional opposition between RhoC and its counterparts in the RhoA subfamily, which can be exploited to strengthen the vascular endothelial barrier.

DISCUSSION

Our findings reveal a surprising divergence in function among the highly similar Rho GTPases, RhoA, RhoB, and RhoC. RhoC exhibits unique regulatory and functional features in human endothelial cells: it is regulated by cell confluency, localizes to and stabilizes cell-cell junctions and junctional actomyosin, and is much more active in homeostatic confluent endothelial cells than the closely related RhoA and RhoB. Importantly, the predominant role of this GTPase represents a novel therapeutic target since it can be exploited to reinforce the endothelial barrier and protect the vasculature, opening promising new avenues for developing treatments against acute pathologies linked to endothelial dysfunction.

In the canonical model of regulation of endothelial barrier function by Rho GTPases, the RhoA subfamily drives contraction and disruption of barrier integrity, whereas Rac subfamily members, namely Rac1, are involved in barrier reformation and maintenance. Disruptive stimuli such as thrombin, LPS and histamine activate RhoA (Gavard and Gutkind, 2008; Marcos-Ramiro et al., 2016; Mikelis et al., 2015; van Nieuw Amerongen et al., 1998) whereas pro-barrier stimuli such as sphingosine-1-phospate and hepatic growth factor activate Rac (Birukova et al., 2007; Garcia et al., 2001; Marcos-Ramiro et al., 2016; Vandenbroucke et al., 2008). However, a dual role in permeability, promoting both pro-barrier and anti-barrier signaling, has already been identified in epithelial cells for the RhoA subfamily, yielding important mechanistic insights (Kakiashvili et al., 2009; Nusrat et al., 1995; Utech et al., 2005). Sahai and Marshall have shown that ROCK is the main effector mediating RhoA-mediated acute contraction and barrier disruption, whereas mDia is the effector involved in the RhoA subfamily-mediated stabilization of epithelial AJs (Sahai and Marshall, 2002). In our experimental settings we have also found that ROCK is involved in acute cell contraction (Fernandez-Martin et al., 2012; Marcos-Ramiro et al., 2016) but, as we show here, is not involved in RhoC-dependent maintenance of endothelial barrier integrity. Instead, MLCK appears to be mediating this latter effect, implying that, in these vascular cells, the signaling pathways also diverge downstream the RhoA subfamily.

A RhoA pro-barrier function already holds significant pathological relevance in intestinal epithelia: RhoA inactivation is a major pathogenic factor that causes loss of barrier integrity in inflammatory bowel disease (Lopez-Posadas et al., 2016). The RhoA signal is impaired in intestinal epithelial cells (IECs) from patients with inflammatory bowel disease (IBD), which causes progressive epithelial barrier dysfunction. Furthermore, conditional loss of RhoA was sufficient to mimic chronic intestinal inflammation, impair intestinal barrier function and provoke an increase in IEC shedding. Although the specific effects of RhoA KO on epithelial cell-cell junctions, cytoskeletal rearrangement and IES permeability were not addressed, treatment with CN03 clearly reduced intestinal inflammation and the IBD score in a genetic model altering RhoA activity (Lopez-Posadas et al., 2016).

Septicemia causes a paradigmatic endothelial barrier disruption that leads to vascular leakage, organ edema and failure, making endothelial barrier function an important therapeutic target (Goldenberg et al., 2011; Reinhart et al., 2017). However, the progress in finding new treatments focused on the host response have been at standstill for the last decade for this pathology. Current strategies of hemodynamic stabilization that directly target the microvasculature are limited to the use of vasopressors, general anti-inflammatory drugs such as corticosteroids that may regulate vascular beds, and other alternative treatments to reduce the inflammatory mediators in the bloodstream (Vincent, 2022; Ronco et al., 2023; Giamarellos-Bourboulis et al., 2024). It is noteworthy that some attempts to reinforce vascular barrier function targeting endothelial molecular scaffolds have been carried out. Imatinib, an inhibitor of Abl kinases, broadly used for cancer treatments, has been found to activate Rac1 and strengthen endothelial cell adhesion to the extracellular matrix and hence, the endothelial barrier function, in preclinical models of sepsis (Aman et al., 2012). Indeed, imatinib has been tested in some clinical trials with moderate positive effects on ameliorating inflammatory systemic diseases such as severe COVID19 (Aman et al., 2021; Duijvelaar et al., 2022). We have compared the effects of imatinib and CN03 on vascular leakage *in vivo* (not shown) and found a similar reduction of hyperpermeability between these two compounds, which suggests that RhoA subfamily of GTPases controls a signaling pathway that that could be exploited as a new therapeutic option to prevent organ damage upon systemic inflammation. Whether RhoC-mediated and Rac1-mediated pathways crosstalk at any point under these circumstances is an open question that needs to be addressed, although we have experimentally addressed the effect of RhoA, RhoB and RhoC silencing on Rac1 activity and found no significant changes. This implies that imatinib and CN03 control parallel signaling routes, opening the possibility of targeting simultaneously both of them and investigate their additive effects.

The early reports on the specific effect of RhoA subfamily member overexpression present somewhat contradictory results. RhoC is more disruptive for cell-cell junctions than exogenous RhoA expression in the human colon epithelial cell line HCT116 (Sahai and Marshall, 2002), whereas RhoC expression reinforces the perijunctional ring in the human colon epithelial cell line T84, suggesting a pro-barrier role for this GTPase (Nusrat et al., 1995). Most of these studies have been performed overexpressing mutants, which increased transversal stress fibers and induced cell contraction, instead of externally modulating endogenous RhoA activity. This suggests that activity turnover and subcellular localization are essential for active endogenous Rho proteins to function correctly. In this respect, and also in the epithelium, the outcome of Rho GTPase activation is known to be strongly determined by its subcellular location. In particular, local, perijunctional RhoA activation supported by junctional myosin-II improves barrier function in epithelia. Such activation close to cell-cell junctions could be prevented by myosin IIa knockdown and myosin inhibition with blebbistatin, which disrupts AJs in a similar way to that we reported for endothelial cells with the MLCK inhibitor ML-7 (Priya et al., 2015). Putting these and our results together, an appealing concept emerges with respect to epithelial and endothelial junctions as mesoscopic hubs that orchestrates differential modulation of Rho signaling by regulating the accessibility of Rho regulators. Junctional protein complexes recruit RhoGEFs (Juettner et al., 2019; Timmerman et al., 2015; Ngok et al., 2012; Acharya et al., 2018; Ngok et al., 2013) and RhoGAPs (Zebda et al., 2013), but they could also prevent the accessibility of these regulators, as it happens for the Rho activity suppressor p190B RhoGAP in columnar epithelial cells (Priya et al., 2015). These accessibility is regulated, for example, by mechanotransduction (Acharya et al., 2018) and may be a relevant target for endothelial hyperpermeability caused by pathological inflammation (Khan et al., 2021; Pierce et al., 2017; Khan et al., 2022)

Considering the importance of endothelial junctions as Rho regulatory cellular domains, we have identified the molecular basis for the functional differences between RhoA and RhoC in confluent human endothelium. The positively charged R188 in RhoC is a S188 in RhoA, which can be phosphorylated by PKA and thus negatively charged (Lang et al., 1996). R188 significantly contributes to target RhoC to cell-cell junctions, thereby allowing this GTPase to gain access to junctional domain enriched in Rho GEFs and perhaps devoid of Rho GAPs. Indeed, the formation of cell-cell junctions upon confluency increases the activity and expression of RhoC, but not of RhoA. This major role of confluency in shifting the balance of expression and activity RhoA and RhoC can have potential consequences in processes involving junctional remodeling such as angiogenesis and vasculogenesis, which should be thoroughly explored in the future.

MATERIALS AND METHODS

KEY RESOURCES TABLE

Antibodies

Antibody	Specie	Reference	Dilution WB	Dilution IF
Anti-myosin light chain (MLC)	Rabbit	Cell Signaling (3672)	1:500	-
Anti-myosin heavy chain II-α	Rabbit	BioLegend (909802)	1:1000	-
Anti-α-catenin	Rabbit	Abcam (EP1793Y)	1:1000	-
Anti-β-catenin	Rabbit	Sigma-Aldrich (c2206)	1:1000	
Anti-Claudin-5 (A-12)	Mouse	Santa Cruz Biotechnology INC. (sc-374221)	1:500	-
Anti-ERK1 (K23)	Rabbit	Santa Cruz Biotechnology INC. (sc-94)	1:1000	-
Anti-MHC-IIa	Mouse	Santa Cruz Biotechnology INC. (sc-53095)	1:100	
9E10	Mouse	ROCHE (11667203001)	1:1000	-
Anti-N-cadherin	Mouse	Sigma Aldrich (C3865)	1:500	-
Anti-OB-cadherin (F-3)	Mouse	Santa Cruz Biotechnology INC. (sc-365867)	1:500	-
Anti-Ocluddin-1 (E-5)	Mouse	Santa Cruz Biotechnology INC. (sc-133256)	1:500	-
Anti-phospho-S19-(p) Myosin light chain (MLC)	Rabbit	Cell Signaling (3671)	1:500	1:100
Anti-p120-catenin (Clone 98)	Mouse	BD Bioscience (610134)	1:1000	-
Anti-Paxillin (Clon 349)	Mouse	BD Bioscience (610051)	1:1000	-
Anti-PECAM-1	Mouse	Santa Cruz Biotechnology INC. (sc-365804)	1:1000	1:100
Anti-PECAM-1	Rabbit	Abcam (ab32457)	1:300	

Anti-Rac1	Mouse	BD Transduction Laboratories (610650)	1:1000	-
Anti-Cdc42 (Clone 44)	Mouse	BD Bioscience (610929)	1:1000	-
Anti-RhoA(26C4)	Mouse	Santa Cruz Biotechnology INC. (sc-418)	1:500	1:100
Anti-RhoB (C5)	Mouse	Santa Cruz Biotechnology INC. (sc-8048)	1:500	1:100
Anti-RhoC (D40E4)	Rabbit	Cell Signaling (3430)	1:1000	1:100
Anti-β-Tubulin	Mouse	Santa Cruz Biotechnology INC. (sc-124241)	1:10000	-
Anti-Cadherin-5 (Clon 75)	Mouse	BD Transduction Laboratories (610252)	1:1000	1:250
Anti-Cadherin-5 (D87F2)	Rabbit	Cell Signaling (25005)	1:1000	1:500
Anti-ZO-1	Rabbit	ThermoFisher (40-2200)	1:1000	-
Anti-RhoGDI	Mouse	Santa Cruz Biotechnology	1:1000	
Anti-GFP	Mouse	Roche (11814460001)	1:4000	
Anti-GAPDH	Mouse	Invitrogen (AM4300)	1:60000	
Anti-IgGs Rabbit 488	Donkey	Invitrogen A-21206	-	1:500
Anti-IgGs Rabbit 555	Donkey	Invitrogen A-31572	-	1:500
Anti-IgGs Rabbit 647	Donkey	Invitrogen A-31573	-	1:200
Anti-IgGs Rabbit HRP	Donkey	GE Healthcare NA934V	1:5000	
Anti-IgGs Mouse 488	Donkey	Invitrogen A-21202	-	1:500
Anti-IgGs Mouse 555	Donkey	Invitrogen A-31570	-	1:500
Anti-IgGs Mouse 647	Donkey	Invitrogen A-31571	-	1:200

Anti-IgGs Mouse HRP	Donkey	Jackson Immunoresearch 715-035-151	1:5000	-

Reagents

Reagent	Reference	Source
Bovine serum albumin (BSA)	A7906	Sigma-Aldrich
Cicloheximide	01810	Sigma-Aldrich
Cysteine	168149	Sigma-Aldrich
CN03	CN03-A	Cytoskeleton
Colagenase	C9407	Sigma-Aldrich
DAPI	268298	Merk
DMEM, high fructose, GlutaMax pyruvate	31966-021	Life Technologies
DMSO	67-68-5a	Sigma-Aldrich
Evans Blue	E2129	Sigma-Aldrich
Phalloidin-Alexa 647	A-22287	Invitrogen
Phalloidin -TRITC	P1951	Sigma-Aldrich
Fibronectin	F0635	Sigma-Aldrich
Fluoromount	0100-01	Southern Biotechnology Asociates Inc.
Formalin	HT501128	Sigma-Aldrich
GI254023X	3995	Tocris
Glutathione-sepharose	17-0756-	01GE Healthcare
Imatinib-mesylate	S1026	Selleckchem
LPS	L8274	Sigma-Aldrich
ML-7	I2764	Sigma-Aldrich
Neutravidin agarose	29201	Thermo Scientific
Oligofectamine	12252011	Invitrogen
Amersham™ ECL Prime	28980926	GE Healthcare
Rho Inhibitor I (C3 transferase)	CT04	Cytoskeleton
Sulfo NHS-biotin	21217	Thermo Scientific
TNF-α	210-TA/CF	RD Systems

Triton X-100	T9284	Sigma-Aldrich
Tween-20	P1379	Sigma-Aldrich
Murine VEGF	450-32	Preprotech
X-tremeGENE™ DNA Transfection Reagent	6365779001	Roche
Y27632	688000	Calbiochem
Accu-Chek Aviva Testrips	06453970	Roche

Plasmids

Plasmid	Backbone	Source
GST	pGEX-2T	Prof. Anne Ridley (University of Bristol, Bristol, UK)
GST-PBD-PAK	PGEX-2T	Prof. Martin A. Schwartz (Yale School of Medicine, New Haven, CT)
GST-RBD-Rtk	pGEX-2T	Prof. Martin A. Schwartz (Yale School of Medicine, New Haven, CT)
PRK5myc-RhoA	pRK5	Prof. Anne Ridley (University of Bristol, Bristol, UK)
PRK5myc-RhoB	pRK5	Prof. Anne Ridley (University of Bristol, Bristol, UK)
PRK5myc-RhoC	pRK5	Prof. Anne Ridley (University of Bristol, Bristol, UK)
RhoC FLARE.sc mCer, mVenus - wt	pTriEx	Addgene (65071)
RhoC FLARE.sc mCer, mVenus – Q63L	pTriEx	Addgene (65424)
RhoC FLARE.sc mCer, mVenus – T19N	pTriEx	Addgene (65423)
VE-cadherin-Dendra2	pEGP-N1	Laboratory
GFP-RhoA	pEGFP-C3	Addgene (23224)

GFP-RhoB	pEGFP-C2	Dr. Dolores Pérez Sala (Centro de Investigaciones Biológicas, Madrid)
GFP-RhoC	pEGFP-C2	Addgene (23226)
GFP-RhoA-S188R	pEGFP-C3	Laboratory
GFP-RhoC-R188S	pEGFP-C2	Laboratory
GFP-RhoC-R188A	pEGFP-C2	Laboratory
GFP-RhoA-hyper	pEGFP-C1	Laboratory
GFP-RhoA-hyper-S188R	pEGFP-C1	Laboratory
GFP-RhoA-hyper-C190G	pEGFP-C1	Laboratory
GFP-RhoC-hyper	pEGFP-C1	Laboratory
GFP-RhoC-hyper-R188S	pEGFP-C1	Laboratory
GFP-RhoC-hyper-C190G	pEGFP-C1	Laboratory

Small interfering RNA (siRNA) oligonucleotides

Target Protein	siRNA	Sequence 5´-3´	Source
RhoA	siRhoA (D-003860-02)	GAACUAUGUGGCAGAUAUC	Dharmacon
RhoB	siRhoB (D-008395-07)	GCAUCCAAGCCUACGACUA	Dharmacon
RhoC	siRhoC1 (D-008555-01)	GGAGAGAGCUGGCCAAGAU	Dharmacon
RhoC	siRhoC2 (D-008555-02)	AUAAGAAGGACCUGAGGCA	Dharmacon
RhoC	siRhoC3 (J-008555-07)	GGACAUGGCGAACCGGAUC	Dharmacon
RhoC	siRhoC4 (J-008555-08)	CUACGUCCCUACUGUCUUU	Dharmacon
Control1	siControl1 (D-001210-01)	AUGUAUUGGCCUGUAUUAGUU	Dharmacon
Control3	siControl3 (D-001810-	UAGCGACUAAACACAUCAA	Dharmacon

01)

Cloning oligonucleotides

Cloning	Oligonucleotide	Sequence 5´-3´
Dendra2	Dendra2-Fw	GGTGGTACCGGTGAACACCCCGGGAATTAACCT
	Dendra2-Rv	GGTGGTGCGGCCGCCTACCACACCTGGCTGGGCAGGGG
VE-cadherin	VE-cadherin-Fw	GGTGGTGAATCCATGCAGAGGCTCATGATG
	VE-cadherin-Rv	GGTGGTACCGGTGGCGGCGGCGGATACAGCAGCTCCTCCCG
GFP-RhoA S188R	RhoA SR-Fw	GCAAGCTAGACGTGGGAAGAAAAACGTGGGTGCCTTGTC
	RhoA SR-Rv	GACAAGGCACCCACGTTTTTCTTCCCACGTCTAGCTTGC
GFP-RhoC R188S	RhoC RS-Fw	ACAAGCGTCGGAGCGGCTGTCCCATTC
	RhoC RS-Rv	GAATGGGACAGCCGCTCCGACGCTTGT
GFP-RhoC R188A	RhoC RA-Fw	CAAGAACAAGCGTCGGGCGGGCTGTCCCATTCTC
	RhoC RA-Rv	GAGAATGGGACAGCCCGCCCGACGCTTGTTCTTG
GFP-RhoA-hyper	RhoA wt tail annealing Fw	TCGAGGCGGCGGCGCTAGACGTGGGAAGAAAAAATCTGG GCCTTGTCTTGTGAG
	RhoA wt tail annealing Rv	TTCTCACAAGACAAGGCACCCAGATTTTTTCTTCCCACGTC GCCGCC
GFP-RhoA-hyper- S188R	RhoA S188R tail annealing Fw	TCGAGGCGGCGGCGCTAGACGTGGGAAGAAAAAAAGGGG GTCTTGTGAG
	RhoA S188R tail annealing Rv	AATTCTCACAAGACAAGGCACCCCCTTTTTTTCTTCCCAC GTCTAGCGCCGCCGCC
GFP-RhoA-hyper- C190G	RhoA C190G tail annealing Fw	AGGCGGCGGCGCTAGACGTGGGAAGAAAAAATCTGGGGG GTCTTGTGAG
	RhoA C190G	AATTCTCACAAGACAAGGCCCCCAGATTTTTTCTTCCCA

	tail annealing Rv	CGTCTAGCGCCGCCGCC
GFP-RhoC-hyper	RhoC wt tail annealing Fw	TCGAGGCGGCGGCGTCCGCAAGAACAAGCGTCGGAGGG GCTGTCCCATTCTCTGAG
	RhoC wt tail annealing Rv	AATTCTCAGAGAATGGGACAGCCCCTCCGACGCTTGTTC TTGCGGACGCCGCCGCC
GFP-RhoC-hyper-R188S	RhoC R188S tail annealing Fw	TCGAGGCGGCGGCGTCCGCAAGAACAAGCGTCGGTCTG GCTGTCCCATTCTCTGAG
	RhoC R188S tail annealing Rv	AATTCTCAGAGAATGGGACAGCCAGACCGACGCTTGTTC TTGCGGACGCCGCCGCC
GFP-RhoC-hyper-C190G	RhoC C190G tail annealing Fw	CGAGGCGGCGGCGTCCGCAAGAACAAGCGTCGGAGGGGCG CCCC ATTCTCTGAG
	RhoC C190G tail annealing Rv	CTCAGAGAATGGGGCCGCCCCTCCGACGCTTGTTCTTGCGG CGCCGCC

qPCR oligonucleotides

Gene (homo sapiens)	Oligonucleotide	Sequence 5´-3´
CDH5	CDH5 IS Fw	GAACCAGATGCACATTGATGA
	CDH5 IS Rv	CGACTCACGCTTGACTTGAT
PECAM-1	PECAM1 IS Fw	CACTGCAGAGTACCAGGTGT
	PECAM1 IS Rv	AGTTGACCCTCACGATCCCA
RPLP	RPLP IS Fw	CACTGAGATCAGGGACATGTTG
	RPLP IS Rv	TGACTTCACATGGGGCAAT
GAPDH	GAPDH Fw	TCTCCTCTGACTTCAACAGCGAC
	GAPDH Rv	CCCTGTTGCTGTAGCCAAATTC
B2M	B2M Fw	GAGTATGCCTGCCGTGTG
	B2M Rv	AATCCAAATGCGGCATCT

- Cell culture and transfection

Human embryonic kidney (HEK) 293 cells were obtained from the American Type Culture Collection and grown in DMEM supplemented with 10% FBS. HUVECs were purchased from Lonza and grown in EGM-2 medium (Lonza). HDMVECs and the corresponding culture medium (CADMEC medium) were purchased from TebuBio and grown according to the manufacturer's instructions. EA.hy.926 cells were grown in DMEM supplemented with 10% FBS in an atmosphere of 5% CO2/95% air. EA.hy.926 cells were a gift from C.J.S. Edgell (University of North Carolina, Chapel Hill, NC). Plates were precoated with 10 µg/ml fibronectin (Sigma-Aldrich) for at least 30 min (plastic) or 2 h (glass coverslips) prior to cell culture. All cell types were grown at 37ºC in an atmosphere of 5% CO2/95% air. Murine lung endothelial cells were isolated as previously described (Colás-Algora et al., 2020). Briefly, mouse lungs were minced and digested with 0.1% type I collagenase solution (Gibco) for 1 h at 37 °C. Lung tissue was further disaggregated with a 19.5 G needle and subsequently filtered through a cell strainer. Lung cell suspension was then subjected to positive sorting with an antibody against the endothelial cell marker ICAM-2 conjugated to magnetic Dynabeads Sheep Anti-Rat IgG (11035) from Thermo Fisher, for 30 min at 4 °C. After extensive washes, endothelial cell rich fraction was lysed with Laemmli sample buffer and subjected to western blot analysis.

For siRNA transfection, HUVEC or HDMVECs were plated at subconfluence ($5x10^5$ cells per 60 mm-dish) in their respective culture media without antibiotics. Cells were transfected 24 h later with a mixture of 8 µl of Oligofectamine (Invitrogen) and the indicated siRNA to a final concentration of 100 nM. 24 h after oligotransfection, cells were trypsinized and plated at confluence in different wells for parallel assays, such as western blotting, immunofluorescence or permeability assays, performed 72 h after transfection.

For DNA transfection, $2x10^5$ cells per well were seeded on 24-well plates containing fibronectin-coated glass coverslips. For time-lapse analysis of living cells, including FRET and photoconversion assays, $2x10^5$ HUVECs were seeded on fibronectin-coated µ-Slide 8 Well chambers (Ibidi). Cells were transfected with a mixture of 1 µg of plasmid DNA and 1 µl X-tremeGENE™ HP DNA Transfection Reagent (Sigma-Aldrich) per well. Medium was replaced 24 h after transfection and experiments were performed 48 h post-transfection.

- Molecular cloning of GFP-hyper constructs

RhoA and RhoC hypervariable regions were added to the C-terminal domain of GFP in a GFP-C1 vector using the using the annealed oligonucleotides listed in the Key Resources Table. The inserted sequences contain one Xho-I site at the 5´end one EcoR1 site at the 3´ end, which allowed the ligation of the annealed oligonucleotides to the GFP plasmid.

- Site-directed mutagenesis of RhoA and RhoC hypervariable regions

The aforementioned mutations in the hypervariable regions of RhoA-GFP and RhoB-GFP were generated according to the manufacturing instructions of the QuickChange Lightning Site-Directed Mutagenesis kit (Agilent Technologies) using the mutagenic primers listed in the Key Resources Table. Plasmid containing the indicated mutations were transformed into XL10-Gold ultracompetent cells. Plasmids from selected colonies were sequenced before scaling up their purification with EndoFree Plasmid Maxi kit (Qiagen) and subsequent transfection.

- qRT-PCR

Oligonucleotides for qPCR are listed in the Key Resource Table. 1 μg RNA from HUVECs was subjected to reverse transcription with the High-Capacity RNA-cDNA kit (Applied Biosystems). RT-qPCR was performed from the resulting cDNA in a CFX 384 thermocycler (Bio-Rad) using the SsoFast EvaGreen Supermix (Bio-Rad) and forward and reverse primers, designed with Probefinder software (Roche). Parallel qPCR assays for the housekeeping genes RPLP and GAPDH and B2M were performed to normalize data from each point. Three replicates of all the samples were run in parallel with non-reverse transcription controls for all the targets, which yielded no detectable amplification. Unless otherwise indicated, the quantification cycle (Cq) values fell in the 20–24 range, which denotes medium to high levels of these transcripts. Results were quantified and represented (2−ΔCq) using GenEx software, correcting for the efficiency of each pair of primers. The analyses were performed in technical triplicates. Contamination with genomic DNA was negligible. Subsequently, these values were normalized with respect to the mean values of housekeeping genes used as reference. The stability of the candidate reference genes was probed with geNorm and Normfinder algorithms within GenEx, and the combination of the two most stable genes was chosen against which to normalize the results.

- Endothelial barrier function assay

Trans-endothelial electric resistance (TEER) assays with an electric cell-substrate impedance sensing system (ECIS 1600R; Applied Biophysics)(Tiruppathi et al., 1992) were performed as described (Colas-Algora et al., 2019; Marcos-Ramiro et al., 2016). TEER indicate the resistance values at 4000 Hz. The Rb, α, and membrane capacitance values (Cm) were modelled using the ECIS software (Applied Biophysics) running the experiment in the multi-frequency mode, which ranges between 250 and 64000 Hz. This mathematical modelling split TEER values into α values, which correlates with focal adhesion formation, Rb values, which reflects paracellular barrier formation (Rb), and Cm, which reflects the membrane capacitance TEER decrease was quantified as the percentage of decrease in the TEER, taking as 100% the difference between the TEER value at t = 0 h and the TEER value of an empty well.

- Western blot

For Western blot analysis, equal amounts of proteins were loaded onto polyacrylamide gels (8-12%) under reducing conditions and transferred to Immobilon-P membranes (EMD Millipore). After blocking with 5% BSA (wt/vol) and 0.05% (vol/vol) Tween-20 in TBS (25 mM Tris, pH 7.4, and 150 mM NaCl), membranes were incubated overnight with the indicated antibodies, washed with TBS containing 0.05% Tween 20, and incubated for 30 min with the corresponding secondary antibodies coupled to HRP. After extensive washes, the signal was visualized with an enhanced chemiluminescense Western blotting kit (ECL; GE Healthcare). Band intensities were quantified using Fiji and the results were represented relative to controls.

- Surface biotinylation assays

HUVECs were plated in 60-mm dishes and incubated with 0.250 mg/ml sulfo-NHS-biotin in PBS supplemented with 1.5 mM Ca^{2+} and Mg^{2+} (PBS-Ca^{2+} Mg^{2+}) for 30 min at 4ºC. Cells were washed with PBS-Ca^{2+} $Mg^{2+}$to eliminate the excess of non-labelled NHS-biotin and incubated for 10 min with DMEM 10% FBS to quench the remaining free NHS-biotin, and then washed again with PBS-Ca^{2+} Mg^{2+}. Cells were lysed with were harvested in lysis buffer (1x TBS, 10 mM EDTA, 1% Triton, 0.3 µg/ml Caliculin A, 1 mM PMSF, 10 µg/ml Aprotinin, Leupeptin and Pepstatin, 1 mM Sodium Orthovanadate, 10 mM β-Glycerol Phosphate, and 10 mM Sodium Fluoride) and passed through a 0.6-mm 24G needle. All of these procedures were performed at at 4ºC. Subsequently, lysates were incubated 5 min at 37ºC and centrifuged at 14,000 rpm for 5 min. Part of the supernatant was conserved as total lysate and the remainder was subjected first to a preclearing step with agarose for 1 h at 4°C and then to pull-down assay with NeutrAvidin agarose (Thermo Scientific) for 2 h at 4°C to isolate biotinylated proteins.

- Activation of endogenous RhoA subfamily of GTPases and pull-down assay for RhoA GTPases activity

HUVECs were grown at confluency for 3 days and starved for 24 h. Cells were incubated with 1.5 µg/ml CN03 for 3 h and then lysed and subjected to pull-down assays to measure GTP-loaded RhoA, RhoB and RhoC, as previously described (Marcos-Ramiro et al., 2016; Ren and Schwartz, 2000). HDMVECs were stimulated with 5 µg/ml CN03 after previous titration assays. Briefly, cell lysates were incubated at

4 °C in assay buffer with 10 µg of glutathione-sepharose beads conjugated with GST-RBD-Rtk to isolate active RhoA, RhoB and RhoC, or conjugated to GST-PBD-PAK to isolate active Rac1 and Cdc42. A fraction of the initial postnuclear supernatants and the final GST pull-down samples were subjected to SDS-PAGE and western blot analysis with the indicated anti-Rho antibodies.

- Laser scanning confocal microscopy

Confluent cells grown on coverslips were fixed in 4% paraformaldehyde (PFA) for 15 min, and rinsed and treated with 10 mM glycine for 2 min to quench the aldehyde groups. Cells were then permeabilized with 0.2% Triton X-100, and rinsed and blocked with 3% bovine serum albumin (BSA) in PBS for 15 min at room temperature (RT). Cells were incubated for 30 min with the primary antibodies, rinsed in PBS, and incubated for 30 min with the appropriate fluorescent secondary antibodies. Actin filaments were detected with fluorophore-conjugated phalloidin (see key resources table). Incubation with antibodies and other fluorescence reagents was always carried out at 37°C. Phosphorylated proteins were stained using Tris-buffered saline (20 mM Tris, pH 7.4; 150 mM NaCl) instead of PBS. Confocal laser scanning microscopy was carried out with a confocal Zeiss LSM710 system coupled to an AxioImager M2 microscope, a confocal Zeiss LSM 800 system coupled to an AxioObserver microscope, and a confocal Nikon AR1+ system coupled to an Eclipse Ti-E microscope. Fiji was used for quantification of the area covered by AJs. Using Z-stacks of endothelial monolayers projected in a single image, a Region Of Interest (ROI) was drawn to encompass the entire cell including the intercellular junctions. This provides us with the total intensity of the protein of interest in the cell as well as the cell area. A smaller adapted ROI was drawn to surround the cell inside beneath the intercellular junctions. Values from the inner area were subtracted from those from the outer, peripheral area, providing a measurement of the percentage of overlapping reticular areas with respect to the cellular area, as well as the junctional distribution of the indicated proteins with respect to the total cellular staining. The average intensity was measured in each region by dividing the RawIntDen value (sum of the pixels in a given region) by the area, allowing for comparison of parameters between different images.

- Generation of VE-cadherin-Dendra2 construct, photoconversion and time-lapse microscopy

VE-cadherin-GFP-N1 vector previously generated in the laboratory from a VE-cadherin expression plasmid kindly donated by Elisabetta Dejana. Photoconvertible VE-cadherin-Dendra2 chimera was generated by substituting the GFP sequence by the Dendra-2 sequence. Briefly, Dendra-2 was amplified by PCR using the oligonucleotides described in the Key Resources Table, containing the Age-1 and Not-1 restriction sites. To study VE-cadherin dynamics, HUVECs were transfected with the expression vector coding for VE-cadherin-Dendra2 in µ-Slide 8 Well (Ibidi). 48 h later and 5 h before photoconversion, the medium was replaced with EBM-2 without phenol red, supplemented with 1% FBS and 10 mM Hepes, pH 7.4. Time-lapse microscopy was performed with a confocal Nikon AR1+ system coupled to an Eclipse Ti-E microscope, in an environmental chamber at 37ºC and an atmosphere of 95% O2/5% CO2. Cells were simultaneously filmed in green (λ = 488 nm) and red (λ = 543 nm). An image was acquired before photoconversion as the initial fluorescence value for both wavelengths. A region of interest (ROI) in cell-cell junctions was then irradiated with a 405-nm laser at 10% power. The ROI underwent an emission shift from 488-nm to 543-nm. Images were acquired every 2 s for 8 min. To analyze the VE-cadherin-Dendra2 experiments, we quantified the mean fluorescence intensity in the photoconverted area over time using Fiji. We extracted disappearance rate constants from exponential curves of VE-cadherin-Dendra2 543-nm intensity decay.

- FRET imaging of RhoC activity

The human endothelial cells Ea.hy.926 were plated in a µ-Slide 8 Well chamber (Ibidi) and transfected with the corresponding RhoC-FLARE. 24 h post-transfection, cells were starved for 24 h in EBM-2 without phenol red, supplemented with 1% FBS and 10 mM HEPES. CN03 was added 3 hours prior to the experiment. Images were acquired in an environmental chamber at 37ºC and an atmosphere of 95% O2/5% CO2, using a wide-arc lamp fluorescence microscope (FRET system). Emission ratio imaging was performed with a 460-500-nm excitation laser/520-550-nm emission YFP. We previously defined the range between the active and inactive states of the biosensor by analyzing FRET efficiency in cells expressing the active and dominant negative forms of RhoC-FLARE. Images were processed and analyzed using Fiji software.

- Transmission electron microscopy and 3D image reconstruction

Confluent human lung microvascular endothelial cells transiently expressing PECAM-1-GFP were in situ fixed with 4% paraformaldehyde and 2% glutaraldehyde in 0.1 M phosphate buffer, pH 7.4 for 2 h at RT. Postfixation was carried out with a mixture of 1% osmium tetroxide and 0.08% potassium ferricyanide for 1 h at 4°C and then with

2% uranyl acetate for 1 h at RT. Samples were dehydrated with ethanol and processed for standard Epon (TAAB-812) embedding. After polymerization, consecutive orthogonal ultrathin sections (70 nm) were collected on formvar-coated slot grids and stained with uranyl acetate and lead citrate. Finally, sections were examined in a Jeol JEM-1400Flash transmission electron microscope operating at 100 kV. Images were recorded with a Gatan OneView (4K x 4K) CMOS camera at 4000x magnification.

For 3D reconstruction, electron microscopy images were binned 4 times, with an effective pixel size at the specimen level of 11.2 nm, and their intensities were normalized to the same mean and standard deviation. The electron microscopy images of the series were mutually aligned with the IMOD software tool (Kremer et al., 1996). To this end, structural features unequivocally identified in adjacent sections, especially membrane invaginations and multivesicular bodies, were manually selected (around 25-30 per each pair of images) and employed as fiducial marks to align each pair of consecutive sections independently. Finally, each section was transformed into a common alignment in which the section located in the middle of the series acted as a reference, resulting in the aligned series and thus yielding the 3D reconstruction. Modelling of the 3D reconstruction was done with IMOD by manually tracing the plasma membranes. The total thickness of the 3D reconstruction consisting of 27 individual sections was around 1.89 μm.

- Intradermal injection of inflammatory stimuli and Miles assay

Female CD-1 mice were intraperitoneally injected with saline or 0.175 mg/kg of CN03. A Miles assay was performed after 3.5 h after injection. Briefly, we depilated the back of the mice and retro-orbitally injected them with 150 μl 0.5% w/v Evans Blue (Merck).

15 min later, saline, 20 μg of LPS and 50 ng of VEGF were intra-dermally injected in the back of each mouse for 15 min. Mice were then euthanized and the stimulated points of the skin, as well as 100 mg of liver, lung and kidney were harvested from each mouse. Evans blue was extracted with formamide at 55 °C for 48 h, measured spectrophotometrically and normalized with respect to the tissue weight.

- LPS-induced systemic inflammation

Female CD-1 mice were intraperitoneally injected with saline as control or 50 μg/g LPS to mimic the final state of sepsis disease in combination or not with 0.175 mg/kg or 0.525 mg/kg (X3) of CN03. A Miles assay was performed 17 h later in the indicated organs as described, which revealed an increase of tissue edema in response to LPS injection. Blood samples were collected before and after the treatment for each animal. TNF and IL-6 were measured by flow cytometry and plasma glucose was measured with Accu-Chek Aviva Testrips (Roche).

- Mass spectrometry analysis of CN03 sequence

CN03 was analyzed by LC-ESI-MSMS mass spectrometry at the Proteomics Service of the National Center for Biotechnology (CSIC, Spain). 1 μg CN03 was run on a 12% denaturing polyacrylamide SDS-PAGE gel. A single gel band was detected and cut, deposited in a 96-well plate, and automatically processed in a Proteineer DP (Bruker Daltonics, Bremen, Germany). The digestion protocol used was described by Shevchenko et al. (Shevchenko et al., 1996) with the following minor variations: gel plugs were first washed with 50 mM ammonium bicarbonate and then with acetonitrile before reduction with 10 mM DTT in 25 mM ammonium bicarbonate; alkylation was performed with 55 mM IAA in 50 mM ammonium bicarbonate. Then, the gel pieces were washed with 50 mM ammonium bicarbonate and 100% acetonitrile, and then dried under a nitrogen stream. Modified porcine trypsin (sequencing grade; Promega, Madison WI) was added at a final concentration of 16 ng/µl or 25 ng/µl, respectively, in 25% acetonitrile, 50 mM ammonium bicarbonate, and digestion was carried out for 6 hours at 37°C. The reaction was stopped by adding 0.5% TFA for peptide extraction. The tryptic peptides were dried by vacuum centrifugation and resuspended in mobile phase A (0.1% formic acid in water) for LC ESI-MSMS. The NanoLC ESI-MSMS analysis of tryptic peptides was performed using an Eksigent 1D Plus nanoLC coupled to a SCIEX 5600 TripleTOF QTOF mass spectrometer. The analytical column used was a reverse-phase C18 silica-based column of 75 µm x 15 cm, particle size of 1.7 µm, and pore size of 100 Å (Waters). The trap column was a PepMap C18 (Dionex, Sunnyvale, California), particle diameter of 5 µm, pore size of 100 Å, connected online with the analytical column. The loading pump supplied a solution of 0.1% trifluoroacetic acid in 98% water/acetonitrile 2% (Merck) at 3 µL/min. The nanoflow pump provided a flow rate of 250 nL/min and operated under gradient elution conditions, using 0.1% formic acid (Fluka, Buchs, Switzerland) in water as mobile phase A and 0.1% formic acid in 100% acetonitrile as mobile phase B. The elution gradient was performed according to the following scheme: isocratic conditions of 96% A: 4% B for 5 min, linear increase to 40% B in 25 min, linear increase to 95% B in 1 min, isocratic conditions of 95% B for 5 min, and return to initial conditions in 10 min. The injection volume was 5 µl. The nanoLC system was coupled via a nano-spray source (SCIEX) to the QTOF mass spectrometer operating in positive ion mode with the capillary voltage set at 2600 V. Data-dependent acquisition allowed sequentially obtaining both full scan (m/z 350-

1250) MS spectra followed by tandem MS CID spectra of the 25 most abundant ions. Dynamic exclusion was applied to prevent the isolation of the same m/z for 20 seconds after its fragmentation.

The MS and MS/MS data obtained were processed using PeakView (SCIEX). For protein identification, MSMS spectra were searched against a UniProtKB (http://www.uniprot.org) database consisting of entries from Proteobacteria (38594387 entries). Database searches were performed using a licensed version of Mascot v.2.4 (www.matrixscience.com; Matrix Science, London, UK). Search parameters were set as follows: carbamidomethyl cysteine as a fixed modification and oxidized methionine and acetyl (protein N-term) as variable modifications. The peptide mass tolerance was set to 25 ppm for MS1 and 0.05 Da for MS/MS spectra, respectively, and 1 missed cleavage was allowed.

- Label-free quantitative proteomics

Tryptic digestion and tandem mass spectrometry analysis. Identical amounts of each replicate were individually digested with trypsin in reducing and alkylating (chloroacetamide) conditions. Tryptic peptides were dried in a speed-vacuum system and desalted using C18 tips. Thereafter, they were subjected to independent LC-MS/MS analysis using a nano liquid chromatography system (Ultimate 3000 nano HPLC system, Thermo Fisher Scientific) coupled to an Orbitrap Exploris 240 mass spectrometer (Thermo Fisher Scientific). Samples (5 µL) were injected on a C18 PepMap trap column (5 µm, 300 µm I.D. x 2 cm, Thermo Scientific) at 20 µL/min, in 0.1% formic acid in water, and the trap column was switched on-line to a C18 PepMap Easy-spray analytical column (2 µm, 100 Å, 75 µm I.D. x 50 cm, Thermo Scientific).

Equilibration was done in mobile phase A (0.1% formic acid in water), and peptide elution was achieved in a 120 min gradient from 4% - 50% B (0.1% formic acid in 80% acetonitrile) at 250 nL/min. Data acquisition was performed in DDA (Data dependent acquisition) mode, in full scan positive mode. Survey MS1 scans were acquired at a resolution of 60,000 at m/z 200, scan range was 375-1200 m/z, with Normalized Automatic Gain Control (AGC) target of 300 % and a maximum injection time (IT) of 45 ms. The top 10 most intense ions from each MS1 scan were selected and fragmented by Higher-energy collisional dissociation (HCD) of 30%. Resolution for HCD spectra was set to 15,000 at m/z 200, with AGC target of 100 % and maximum ion injection time of 80 ms. Precursor ions with single, unassigned, or six and higher charge states from fragmentation selection were excluded.

Protein identification and label-free protein quantitation analysis. Raw files were processed using Proteome Discoverer (PD) version 2.5 (Thermo Fisher Scientific). MS2 spectra were searched using a combination of four search engines (Mascot v2.7, MSFragger, Amanda and Sequest), against a target/decoy database built from sequences corresponding to the *Homo sapiens* reference proteome downloaded from Uniprot Knowledge database. Database included typical laboratory contaminants. Search parameters considered fixed carbamidomethyl modification of cysteine, and the following variable modifications: methionine oxidation, possible pyroglutamic acid from glutamine at the peptide N-terminus and acetylation of the protein N-terminus. The peptide precursor mass tolerance was set to 10 ppm and MS/MS tolerance was 0.02 Da, allowing for up to two missed tryptic cleavage sites. Spectra recovered by a False Discovery Rate (FDR) <= 0.01 filter were selected and the signals corresponding to each identified peptide were extracted, normalized, assigned by protein inference to their corresponding proteins and used for quantitative analysis. Label-free Protein quantification used unique + razor peptides. The abundance parameter, which correlates with the sum of the intensities of the peptides identified for each protein was analyzed to establish significant changes in protein expression.

- Patient Samples and Study Approval

The study was approved by the local Ethics Committee (La Paz University Hospital, Madrid, PI-4100 version 2, 2020). All the participants provided written consent and the data were treated according to recommended criteria of confidentiality, following the ethical guidelines of the 1975 Declaration of Helsinki. Patients >18 years who met the diagnostic criteria for sepsis according to the Third International Consensus Definitions for Sepsis and Septic-Shock (Singer et al., 2016) were enrolled in this study on arrival at Accident and Emergency Service of La Paz University Hospital. Healthy volunteers were recruited from the Blood Donor Services of La Paz University Hospital. Details of the blood collection, serum preparation and circulating levels of cytokines were described in detail elsewhere (Colás-Algora et al., 2023).

- Statistical analysis

Data from at least three independent experiments are expressed as the mean and standard error of the mean (SEM). An unpaired Student’s t-test or two-way ANOVAs were used to establish the statistical significance ($p < 0.05$) of group differences between the means using Prism 7.0 software. Data were obtained from at least three independent experiments.

AUTHOR CONTRIBUTIONS

N.C-A. and J.M. contributed to the conception and experimental design. N.C-A., P.M-P., M.G-F., A.C., C.C-N., S.B. and G.dR. performed the experiments and acquired the data. M.G-F carried out the RhoC-FRET FLARE analysis. N.C-A., A.C. and C.R. carried out all the *in vivo* experiments. N.C-A. and C.C-N. carried out the photoconversion assays. A.P. performed all the proteomic analyses. J.J.F. performed the 3D reconstruction of the EM images. N.C.A. and J.M. analyzed the data. E.L-C. M.F. and I.J-A. provided material support and reviewed the manuscript. J.M. wrote the manuscript.

ACKNOWLEDGMENTS

The expert technical advices of the confocal microscopy, electron microscopy, genomic and animal facilities are gratefully acknowledged. The work was supported by grants PID2020-119881RB-I00 from AEI (to CC-N, PM-P, NC-A, SB, GdR, GC-T, and JM) and Grant TomoXliver2, Ref: S2022/BMD-7232 funded by Comunidad Autónoma de Madrid. (to SB and JM), and IND2019/BMD-17139 (to GC-T and JM) from Comunidad de Madrid. This research work was also funded by the European Commission─NextGenerationEU (Regulation EU 2020/2094), through CSIC's Global Health Platform (PTI Salud Global) (to JM). SB is also supported by Endocornea2, Convenio Colaboración CSIC, funded by Instituto de Investigación Fundación Jiménez Díaz. The authors also thank Dr Phil Mason, who provided English language support. The authors declare that no conflicts of interest exist.

REFERENCES

Acharya, B.R., A. Nestor-Bergmann, X. Liang, S. Gupta, K. Duszyc, E. Gauquelin, G.A. Gomez, S. Budnar, P. Marcq, O.E. Jensen, Z. Bryant, and A.S. Yap. 2018. A Mechanosensitive RhoA Pathway that Protects Epithelia against Acute Tensile Stress. *Developmental Cell*. 47:439-452.e6. doi:10.1016/j.devcel.2018.09.016.

Agarwal, P., and R. Zaidel-Bar. 2019. Principles of Actomyosin Regulation In Vivo. *Trends Cell Biol*. 29:150–163. doi:10.1016/j.tcb.2018.09.006.

Aktories, K., and A. Hall. 1989. Botulinum ADP-ribosyltransferase C3: a new tool to study low molecular weight GTP-binding proteins. *Trends Pharmacol Sci*. 10:415–8.

Aman, J., J. van Bezu, A. Damanafshan, S. Huveneers, E.C. Eringa, S.M. Vogel, A.B.J. Groeneveld, A. Vonk Noordegraaf, V.W.M. van Hinsbergh, and G.P. van Nieuw Amerongen. 2012. Effective Treatment of Edema and Endothelial Barrier Dysfunction With Imatinib. *Circulation*. 126:2728–2738. doi:10.1161/CIRCULATIONAHA.112.134304.

Aman, J., E. Duijvelaar, L. Botros, A. Kianzad, J.R. Schippers, P.J. Smeele, S. Azhang, I.H. Bartelink, A.A. Bayoumy, P.M. Bet, et al. 2021. Imatinib in patients with severe COVID-19: a randomised, double-blind, placebo-controlled, clinical trial. *Lancet Resp Med*. 9:957–968. doi:10.1016/S2213-2600(21)00237-X.

Amerongen, G.P. van N., S. van Delft, M.A. Vermeer, J.G. Collard, and V.W.M. van Hinsbergh. 2000. Activation of RhoA by Thrombin in Endothelial Hyperpermeability. *Circ Res*. 87:335–340. doi:10.1161/01.RES.87.4.335.

Bagci, H., N. Sriskandarajah, A. Robert, J. Boulais, I.E. Elkholi, V. Tran, Z.-Y. Lin, M.-P. Thibault, N. Dubé, D. Faubert, D.R. Hipfner, A.-C. Gingras, and J.-F. Côté. 2020. Mapping the proximity interaction network of the Rho-family GTPases reveals signalling pathways and regulatory mechanisms. *Nat Cell Biol*. 22:120–134. doi:10.1038/s41556-019-0438-7.

Colás-Algora, N., D. García-Weber, C. Cacho-Navas, S. Barroso, A. Caballero, C. Ribas, I. Correas, and J. Millán. 2020. Compensatory increase of VE-cadherin expression through ETS1 regulates endothelial barrier function in response to TNFα. *Cell Mol Life Sci*. 77:2125–2140. doi:10.1007/s00018-019-03260-9.

Colás-Algora, N., P. Muñoz-Pinillos, C. Cacho-Navas, J. Avendaño-Ortiz, G. De Rivas, S. Barroso, E. López-Collazo, and J. Millán. 2023. Simultaneous Targeting of IL-1–Signaling and IL-6–Trans-Signaling Preserves Human Pulmonary Endothelial Barrier Function During a Cytokine Storm. *Arterioscler Thromb Vasc Biol*. ATVBAHA.123.319695. doi:10.1161/ATVBAHA.123.319695.

Duijvelaar, E., J.R. Schippers, P.J. Smeele, M.A. De Raaf, A.L.E.M. Vanhove, S.G. Blok, J.W.R. Twisk, A.V. Noordegraaf, F.S. De Man, H.J. Bogaard, and J. Aman. 2022. Long-term clinical outcomes of COVID-19 patients treated with imatinib. *Lancet Resp Med*. 10:e34–e35. doi:10.1016/S2213-2600(22)00052-2.

Fajgenbaum, D.C., and C.H. June. 2020. Cytokine Storm. *N Engl J Med*. 383:2255–2273. doi:10.1056/NEJMra2026131.

Fernandez-Martin, L., B. Marcos-Ramiro, C.L. Bigarella, M. Graupera, R.J. Cain, N. Reglero-Real, A. Jimenez, E. Cernuda-Morollon, I. Correas, S. Cox, et al.. 2012. Crosstalk between reticular adherens junctions and platelet endothelial cell adhesion molecule-1 regulates endothelial barrier function. *Arterioscler Thromb Vasc Biol*. 32:e90–e102. doi:10.1161/ATVBAHA.112.252080.

Giamarellos-Bourboulis, E.J., A.C. Aschenbrenner, M. Bauer, C. Bock, T. Calandra, I. Gat-Viks, E. Kyriazopoulou, M. Lupse, G. Monneret, P. Pickkers, et al. 2024. The pathophysiology of sepsis and precision-medicine-based immunotherapy. *Nat Immunol*.

25:19–28. doi:10.1038/s41590-023-01660-5.
Goldenberg, N.M., B.E. Steinberg, A.S. Slutsky, and W.L. Lee. 2011. Broken barriers: a new take on sepsis pathogenesis. *Sci Transl Med*. 3:88ps25. doi:10.1126/scitranslmed.3002011.
Heissler, S.M., and D.J. Manstein. 2013. Nonmuscle myosin-2: mix and match. *Cell Mol Life Sci*. 70:1–21. doi:10.1007/s00018-012-1002-9.
Hoffmann, C., K. Aktories, and G. Schmidt. 2007. Change in Substrate Specificity of Cytotoxic Necrotizing Factor Unmasks Proteasome-independent Down-regulation of Constitutively Active RhoA *. *J Biol Chem*. 282:10826–10832. doi:10.1074/jbc.M610451200.
Holzner, S., S. Bromberger, J. Wenzina, K. Neumüller, T.-M. Holper, P. Petzelbauer, W. Bauer, B. Weber, and K. Schossleitner. 2021. Phosphorylated cingulin localises GEF-H1 at tight junctions to protect vascular barriers in blood endothelial cells. *J Cell Sci* 134:jcs258557. doi:10.1242/jcs.258557.
Juettner, V.V., K. Kruse, A. Dan, V.H. Vu, Y. Khan, J. Le, D. Leckband, Y. Komarova, and A.B. Malik. 2019. VE-PTP stabilizes VE-cadherin junctions and the endothelial barrier via a phosphatase-independent mechanism. *J Cell Biol*. 218:1725–1742. doi:10.1083/jcb.201807210.
Khan, A., W. Ni, T. Baltazar, F. Lopez-Giraldez, J.S. Pober, and R.W. Pierce. 2022. ArhGEF12 activates Rap1A and not RhoA in human dermal microvascular endothelial cells to reduce tumor necrosis factor-induced leak. *FASEB J*. 36. doi:10.1096/fj.202101873RR.
Khan, A., W. Ni, F. Lopez-Giraldez, M.S. Kluger, J.S. Pober, and R.W. Pierce. 2021. Tumor necrosis factor-induced ArhGEF10 selectively activates RhoB contributing to human microvascular endothelial cell tight junction disruption. *FASEB J*. 35. doi:10.1096/fj.202002783RR.
Klomp, J.E., M. Shaaya, J. Matsche, R. Rebiai, J.S. Aaron, K.B. Collins, V. Huyot, A.M. Gonzalez, W.A. Muller, T.-L. Chew et al. 2019. Time-Variant SRC Kinase Activation Determines Endothelial Permeability Response. *Cell Chem Biol*. 26:1081-1094.e6. doi:10.1016/j.chembiol.2019.04.007.
Kremer, J.R., D.N. Mastronarde, and J.R. McIntosh. 1996. Computer Visualization of Three-Dimensional Image Data Using IMOD. *J Struct Biol*. 116:71–76. doi:10.1006/jsbi.1996.0013.
Lang, P., F. Gesbert, M. Delespine-Carmagnat, R. Stancou, M. Pouchelet, and J. Bertoglio. 1996. Protein kinase A phosphorylation of RhoA mediates the morphological and functional effects of cyclic AMP in cytotoxic lymphocytes. *EMBO J*. 15:510–519.
Mahlandt, E.K., S. Palacios Martínez, J.J. Arts, S. Tol, J.D. Van Buul, and J. Goedhart. 2023. Opto-RhoGEFs, an optimized optogenetic toolbox to reversibly control Rho GTPase activity on a global to subcellular scale, enabling precise control over vascular endothelial barrier strength. *eLife*. 12:RP84364. doi:10.7554/eLife.84364.
Marcos-Ramiro, B., D. Garcia-Weber, S. Barroso, J. Feito, M.C. Ortega, E. Cernuda-Morollon, N. Reglero-Real, L. Fernandez-Martin, M.C. Duran, M.A. Alonso, I. et al. 2016. RhoB controls endothelial barrier recovery by inhibiting Rac1 trafficking to the cell border. *J Cell Biol*. 213:385–402. doi:10.1083/jcb.201504038.
Mikelis, C.M., M. Simaan, K. Ando, S. Fukuhara, A. Sakurai, P. Amornphimoltham, A. Masedunskas, R. Weigert, T. Chavakis, R.H. Adams, S. et al. 2015. RhoA and ROCK mediate histamine-induced vascular leakage and anaphylactic shock. *Nat Commun*. 6:6725. doi:10.1038/ncomms7725.
Ngok, S.P., R. Geyer, A. Kourtidis, N. Mitin, R. Feathers, C. Der, and P.Z. Anastasiadis. 2013. TEM4 is a junctional Rho GEF required for cell–cell adhesion,

monolayer integrity and barrier function. *J Cell Sci*. 126:3271–3277. doi:10.1242/jcs.123869.

Ngok, S.P., R. Geyer, M. Liu, A. Kourtidis, S. Agrawal, C. Wu, H.R. Seerapu, L.J. Lewis-Tuffin, K.L. Moodie, D. Huveldt, et al. 2012. VEGF and Angiopoietin-1 exert opposing effects on cell junctions by regulating the Rho GEF Syx. *J Cell Biol*. 199:1103–1115. doi:10.1083/jcb.201207009.

van Nieuw Amerongen, G.P., M.A. Vermeer, and V.W. van Hinsbergh. 2000. Role of RhoA and Rho kinase in lysophosphatidic acid-induced endothelial barrier dysfunction. *Arterioscler Thromb Vasc Biol*. 20:E127-133. doi:10.1161/01.atv.20.12.e127.

Ortega, M.C., D. Santander-García, B. Marcos Ramiro, S. Barroso, S. Cox, I. Jiménez-Alfaro, and J. Millán. 2016. Activation of Rac1 and Rhoa preserve corneal endothelial barrier function. *Invest Ophthalmol Vis Sci.* 57(14):6210-6222. doi: 10.1167/iovs.16-20031.

Oya, R., O. Tsukamoto, T. Sato, H. Kato, K. Matsuoka, K. Oshima, T. Kamakura, Y. Ohta, T. Imai, S. Takashima, et al. 2021. Phosphorylation of MYL12 by Myosin Light Chain Kinase Regulates Cellular Shape Changes in Cochlear Hair Cells. *J Assoc Res Otolaryngol*. 22:425–441. doi:10.1007/s10162-021-00796-1.

Park, I., C. Han, S. Jin, B. Lee, H. Choi, J.T. Kwon, D. Kim, J. Kim, E. Lifirsu, W.J. Park, et al. 2011. Myosin regulatory light chains are required to maintain the stability of myosin II and cellular integrity. *Biochem J* 434:171–180. doi:10.1042/BJ20101473.

Pierce, R.W., J. Merola, J.P. Lavik, M.S. Kluger, A. Huttner, M.K. Khokha, and J.S. Pober. 2017. A p190BRhoGAP mutation and prolonged RhoB activation in fatal systemic capillary leak syndrome. *J Exp Med*. 214:3497–3505. doi:10.1084/jem.20162143.

Priya, R., G.A. Gomez, S. Budnar, S. Verma, H.L. Cox, N.A. Hamilton, and A.S. Yap. 2015. Feedback regulation through myosin II confers robustness on RhoA signalling at E-cadherin junctions. *Nat Cell Biol*. 17:1282–1293. doi:10.1038/ncb3239.

Pronk, M.C.A., J.S.M. van Bezu, G.P. van Nieuw Amerongen, V.W.M. van Hinsbergh, and P.L. Hordijk. 2019. RhoA, RhoB and RhoC differentially regulate endothelial barrier function. *Small GTPases*. 10:466–484. doi:10.1080/21541248.2017.1339767.

Reglero-Real, N., L. Pérez-Gutiérrez, A. Yoshimura, L. Rolas, J. Garrido-Mesa, A. Barkaway, C. Pickworth, R.S. Saleeb, M. Gonzalez-Nuñez, S.N. Austin-Williams, et al. 2021. Autophagy modulates endothelial junctions to restrain neutrophil diapedesis during inflammation. *Immunity*. 54:1989-2004.e9. doi:10.1016/j.immuni.2021.07.012.

Reinhard, N.R., S.F. van Helden, E.C. Anthony, T. Yin, Y.I. Wu, J. Goedhart, T.W. Gadella, and P.L. Hordijk. 2016. Spatiotemporal analysis of RhoA/B/C activation in primary human endothelial cells. *Sci Rep*. 6:25502. doi:10.1038/srep25502.

Ridley, A.J. 2013. RhoA, RhoB and RhoC have different roles in cancer cell migration. *J Microsc*. 251:242–249. doi:10.1111/jmi.12025.

Rittirsch, D., M.A. Flierl, and P.A. Ward. 2008. Harmful molecular mechanisms in sepsis. *Nat Rev Immunol*. 8:776–787. doi:10.1038/nri2402.

Ronco, C., L. Chawla, F. Husain-Syed, and J.A. Kellum. 2023. Rationale for sequential extracorporeal therapy (SET) in sepsis. *Crit Care*. 27:50. doi:10.1186/s13054-023-04310-2.

Santander-García, D., M.C. Ortega, S. Benito-Martínez, S. Barroso, I. Jiménez-Alfaro, and J. Millán. 2016. A human cellular system for analyzing signaling during corneal endothelial barrier dysfunction. *Exp Eye Res*. 153:8–13. doi:10.1016/j.exer.2016.09.010.

Shevchenko, A., M. Wilm, O. Vorm, and M. Mann. 1996. Mass Spectrometric Sequencing of Proteins from Silver-Stained Polyacrylamide Gels. *Anal. Chem.* 68:850–

858. doi:10.1021/ac950914h.
Singer, M., C.S. Deutschman, C.W. Seymour, M. Shankar-Hari, D. Annane, M. Bauer, R. Bellomo, G.R. Bernard, J.-D. Chiche, C.M. Coopersmith, et al. 2016. The Third International Consensus Definitions for Sepsis and Septic Shock (Sepsis-3). *JAMA*. 315:801–810. doi:10.1001/jama.2016.0287.
Teuwen, L.-A., V. Geldhof, A. Pasut, and P. Carmeliet. 2020. COVID-19: the vasculature unleashed. *Nat Rev Immunol*. 20:389–391. doi:10.1038/s41577-020-0343-0.
Timmerman, I., N. Heemskerk, J. Kroon, A. Schaefer, J. van Rijssel, M. Hoogenboezem, J. van Unen, J. Goedhart, T.W.J. Gadella, T. Yin, Y. Wu, S. Huveneers, and J.D. van Buul. 2015. A local VE-cadherin and Trio-based signaling complex stabilizes endothelial junctions through Rac1. *J Cell Sci*. 128:3514–3514. doi:10.1242/jcs.179424.
Tzima, E., M. Irani-Tehrani, W.B. Kiosses, E. Dejana, D.A. Schultz, B. Engelhardt, G. Cao, H. DeLisser, and M.A. Schwartz. 2005. A mechanosensory complex that mediates the endothelial cell response to fluid shear stress. *Nature*. 437:426–431. doi:10.1038/nature03952.
Vandenbroucke, E., D. Mehta, R. Minshall, and A.B. Malik. 2008. Regulation of Endothelial Junctional Permeability. *Ann N Y Acad Sci*. 1123:134–145. doi:10.1196/annals.1420.016.
Vincent, J.-L. 2022. Current sepsis therapeutics. *eBioMedicine*. 86:104318. doi:10.1016/j.ebiom.2022.104318.
Zebda, N., Y. Tian, X. Tian, G. Gawlak, K. Higginbotham, A.B. Reynolds, A.A. Birukova, and K.G. Birukov. 2013. Interaction of p190RhoGAP with C-terminal Domain of p120-catenin Modulates Endothelial Cytoskeleton and Permeability. *J Biol Chem*. 288:18290–18299. doi:10.1074/jbc.M112.432757.

FIGURE LEGENDS

Figure 1. CN03 activates RhoA, RhoB and RhoC, increases reticular AJs and reinforces endothelial barrier function. (A) Confluent HUVECs were exposed or not to 1.5 μg/ml CN03 for 3 h, lysed and the indicated active GTPases were detected by pull-down assays. **(B and C)** Confluent HUVECs (B) or HDMVEC (C) were exposed to 1.5 μg/ml or 5 μg/ml CN03, respectively, for 3 h, fixed and stained for VE-cadherin and PECAM-1. Right images show two-fold enlargements of the squared areas highlighting the morphology of linear (top) and reticular (bottom) AJs. Bottom plots show quantification of junctional VE-cadherin and PECAM-1 levels and the percentage of reticular AJs area. Scale bars, 50 μm. **(D and E)** Protein expression changes of PECAM-1 and VE-cadherin in HUVECs (D) and HDMVEC (E) exposed to CN03 as in B and C. **(F)** CN03 induces surface localization of PECAM-1 and VE-cadherin Surface-biotinylated proteins were isolated by pull-down assay with NeutrAvidin-agarose in HUVECs exposed or not to CN03 as in A. VE-cadherin and PECAM-1 protein levels from the pull-down fraction were compared with total protein levels from the lysates by western blot analysis. Non-biotinylated cells were analyzed in parallel as a control of the pulldown assay. Immunoblots of tubulin are shown as loading controls. Plots show the mean ± SEM from at least three independent experiments. **(G)** TEER analysis with an ECIS system of HDMVEC exposed to 5 μg/ml CN03. *, $P < 0.05$; **, $P < 0.01$; *** $P < 0.001$.

Figure 2. CN03 stabilizes VE-cadherin preferentially at reticular AJs, which are formed at overlapping junctional areas. (A-C) Confluent HUVECs expressing photoconvertible VE-cadherin-Dendra2 were treated with 1.5 μg/ml CN03 for 3h, then photoconverted at cell-cell junctions and subjected to time-lapse confocal analysis for 8 min (A). Scale bar, 30 μm. Fluorescence decrease in the photoconverted area was calculated as percentage of maximum fluorescence detected at 543 nm at time 0 (B) and from these values the constant of fluorescence reduction was calculated (C). In accordance with the morphological distribution of VE-cadherin-Dendra2, regions were classified as linear or reticular. At least 12 cells per condition were photoconverted in 3 independent experiments. *, $P < 0.05$. **(D)** 3D reconstruction of consecutive transmission electron microscopy sections of microvascular endothelial cells reveals that reticular junctions are formed by overlapping junctional plasma membranes enriched in intertwined invaginations. Top images show representative micrographs of the 27 sections. Bottom images show the 3D modelling from the boxed area in the top images. In the model, plasma membranes of different cells are delineated in different colors and their cytoplasms in semi-transparent textures. White and yellow arrows point at invaginations detected between two different overlapping cells. Scale bar in electron microscopy micrographs, 5 μm. Scale bar in the 3D reconstruction, 2 μm

Figure 3. CN03 protects human endothelial barrier from pathological inflammatory stimuli. (A) TEER and Rb measurements of confluent HDMVECs exposed to bacterial LPS and 3 h later treated or not with 5 μg/ml CN03. Bottom plots show the quantification of TEER decrease after 10 h of LPS stimulation. **(B)** Confluent HDMVEC were incubated with LPS and CN03 as in A, fixed and stained for VE-cadherin, PECAM-1 and F-actin. Bottom left and central plots show the quantification of junctional VE-cadherin and PECAM-1 levels. Bottom right plot shows the quantification of intercellular gaps identified by automatic image processing with Fiji **(C)** Confluent HLMVEC were exposed to 30% sera from healthy donors or sera from patients suffering severe sepsis and TEER was measured with an ECIS system for 48 h. 30% FBS was used as control. **(D and E)**. Endothelial cells were exposed or not to septic sera with or without CN03 for 24 h, fixed and stained for VE-cadherin, PECAM-1 and F-actin. Intercellular gaps were identified by automatic image processing with Fiji and quantified (E). Plots show the mean ± SEM of cell quantifications from at least three independent experiments. Scale bars, 50 μm. *, $P< 0.05$; *** $P<0.001$.

Figure 4. CN03 reduces local and systemic edema and circulating cytokines in response to LPS injection. (A) Representative images of mouse skin locally injected with 20 μg LPS, 50 ng VEGF, or saline serum, 4 h after intra-peritoneal injection of saline serum or 0.175 mg/kg CN03, and 15 min after retro-orbital injection of Evans Blue (EB). Right plots. EB was extracted from skin patches and quantified relative to values of saline-injected patches. Nine animals per condition were used **(B and C).** Blood was initially collected for cytokine and glucose analyses. Mice were then intra-peritoneally injected with saline, LPS+saline, LPS + 0.175 mg/kg CN03 and LPS + 0.525 mg/kg (CN03x3) for 3.5 h, EB was retro-orbitally injected for 15 min and blood was collected again to the measured IL-6 and TNF-α in plasma (B). Animals were sacrificed and vascular leakage was measured by quantifying optical density (O.D.) of EB at 595 nm in 100 mg of tissue. (B) The graph shows the differences (Δ) in cytokine concentration in blood measured after the injection of LPS, compared to the values obtained before the injection, for each of the mice. Dotted line shows mean values of mice intra-peritoneally injected with saline serum. Plots show the mean ± SEM. Five animals per condition were used. *, $P< 0.05$; **, $P< 0.01$; *** $P<0.001$.

Figure 5. Pro-barrier RhoC mediates the protective effect of CN03 on endothelial integrity. (A) Compensatory changes of expression of RhoA subfamily members upon single knockdown of RhoA, RhoB and RhoC **(B)** TEER and normalized Rb values of HUVECs transfected with the indicated siRNA for 72 h. **(C)** Confocal analyses of HUVECs transfected with the indicated siRNA for 72 h, exposed to CN03 or not for 3 h, fixed and stained for VE-cadherin, PECAM-1 and F-actin. **(D)** Relative quantification of VE-cadherin and PECAM-1 intensity at junctions. **(E)** Compensatory expression changes of the remaining RhoA subfamily member after double knockdown of the other two. Double knockdowns generate cells expressing almost only one RhoA subfamily GTPase (only RhoA, only RhoB, only RhoC). **(F)** Increased junctional PECAM-1 and reticular AJs in only RhoC cells with respect to siControl cells. **(G)** Reduced hyperpermeability to LPS, measured as Rb, in only RhoC cells, which are more sensitive to the effect of CN03. Plots show the mean ± SEM from at least three independent experiments. *, $P< 0.05$; **, $P< 0.01$; *** $P<0.001$.

Figure 6. RhoC specifically regulates perijunctional actomyosin. (A) Label-free quantitative proteomics of HUVECs transfected with the indicated siRNAs for 72 h. Volcano plots show the reduction of RhoC detected by quantitative proteomics as experimental control. **(B)** Normalized abundance of myosin-II components detected by quantitative proteomics. **(C)** Reduction of MLC and pMLC expression in HUVECs transfected with the indicated siRNAs for 72 h. Right graph shows quantification of the relative levels of MLC with respect to siControl cells. **(D)** Distribution of F-actin and p-MLC in confluent HUVECs transfected with the indicated siRNAs. Bottom graphs show the intensity profiles for VE-cadherin (green), p-MLC (magenta) and F-actin (black) corresponding to the squared areas in the images. Scale bar, 50 µm. **(E)** Quantification of total and peripheral F-actin and p-MLC intensities **(F)** F-actin and junctional distribution in control and only RhoC HUVECs. Arrowhead point at junctional actin bundles. Bottom graphs show the intensity profiles for VE-cadherin (green) and F-actin (black) corresponding to the squared areas in the images. Right graphs quantify total and perijunctional F-actin levels. Scale bar, 50 µm. **(G)** F-actin and junctional distribution in Control and CN03-treated cells. Arrowhead point at junctional actin bundles. Bottom graphs show the intensity profiles for VE-cadherin (green) and F-actin (black) corresponding to the squared areas in the images. Right graphs quantify total and perijunctional F-actin levels. Scale bar, 50 µm. Plots and graphs show the mean ± SEM from at least three independent experiments. *, P< 0.05; **, P< 0.01; *** P<0.001.

Figure 7. RhoC is preferentially active at cell-cell junctions and is the most active GTPase of the RhoA subfamily in homeostatic conditions. (A) Relative activation levels of RhoA, RhoB y RhoC in unstimulated confluent HUVECs. Tubulin is shown as loading control. Right graphs show quantification of Rho activation with respect to activation levels of RhoA **(B)** RhoC, but not RhoA and RhoB, is detected associated to the surface plasma membrane proteins. (C) Association of RhoA and RhoC to RhoGDI. Confluent HUVECs were lysed and subjected to immunoprecipitation with antibodies specific for RhoA and RhoC. Tubulin is shown as loading control. Bottom plots quantifies the relative levels of GDI association to RhoA and RhoC in the immunoprecipitates. **(D)** Relative expression levels of RhoA, RhoB, and RhoC in mouse lung endothelial cells (MLEC). Three different lysates of HEK293 cells containing similar levels of exogenous RhoA, RhoB, or RhoC tagged with myc were generated as internal standards (left). Three different lysates of MLEC, together with the HEK293 lysate containing the corresponding exogenous myc-Rho (right), were blotted with antibodies against RhoA, RhoB, or RhoC. The expression level of each endogenous Rho protein in the MLEC lysates was then normalized to the intensity signal of their corresponding standard lysate, so the relative abundance of RhoB and RhoC could be quantified and represented with respect to RhoA protein expression (right graph). **(E)** HUVECs were cultured at subconfluency or confluency for 72 h, lysed and subjected to pull-down assays with GST or GST conjugated to the rho binding domain (RBD) of rhotekin to detect active RhoA and RhoC. VE-cadherin is shown as a positive control of confluency-regulated protein expression. Tubulin is shown as a loading control. **(F)** HUVECs were cultured at confluency for 72 h, exposed to not to CN03 for 3h, fixed and stained for RhoC (top images, inverted color) and VE-cadherin. Nuclei were stained with DAPI. Bottom images show a three-fold enlargement of the squared areas. Bottom graphs show the intensity profiles of the discontinuous lines in the enlarged images. Scale bar, 50 µm **(G)** FRET analysis of RhoC-FLARE in the presence or absence of 1.5 µg/ml CN03. Bottom images show

quantification of the FRET signal increase in different cellular regions. Plots show the mean ± SEM from at least three independent experiments. *, P< 0.05; **, P< 0.01; *** P<0.001.

Figure 8. The pro-barrier role of RhoC is regulated by a R188 residue in the hypervariable region, which is not present in RhoA. (A) Cartoon showing chimeric constructs of GFP conjugated to the RhoA and RhoC hypervariable regions (GFP-Rho-hyper). RhoA contains a S residue two positions upstream the prenylation site, whereas RhoC contains a R residue. GFP-RhoA-hyper and GFP-RhoC-hyper containing the wild type hypervariable regions, as well as mutated sequences in which the RhoA S residue was substituted by R (GFP-RhoA-hyper^{S188R}) and the RhoC R residue replaced by S (GFP-RhoC-hyper^{R188S}) were expressed in HUVECs for 24 h, cells fixed and stained for VE-cadherin. Bottom left plots show the Manders' coefficients for GFP-hyper chimeras and VE-cadherin. **(B)** The RhoC R residue was substituted by S or the uncharged amino acid A in GFP-RhoC constructs. Expression plasmids containing the indicated chimeras were ectopically expressed for 24 h, cells were fixed, stained for VE-cadherin and junctional co-localization quantified with Manders' coefficient. **(C)** HUVECs expressing the indicated GFP-Rho proteins for 48 h were lysed and subjected to pull-down assays with GST-RTK to detect GTP-loaded RhoA and RhoC. Total and active fractions were immunoblotted with the indicated antibodies. Right graph shows the relative quantification of GFP-Rho activation with respect to GFP-RhoC activity. **(D)** HUVECs transiently expressing the indicated GFP-Rho proteins were plated on ECIS arrays for 48 h and TEER and Rb analyzed. Plots show the mean ± SEM from at least three independent experiments. *, P< 0.05; **, P< 0.01; *** P<0.001.

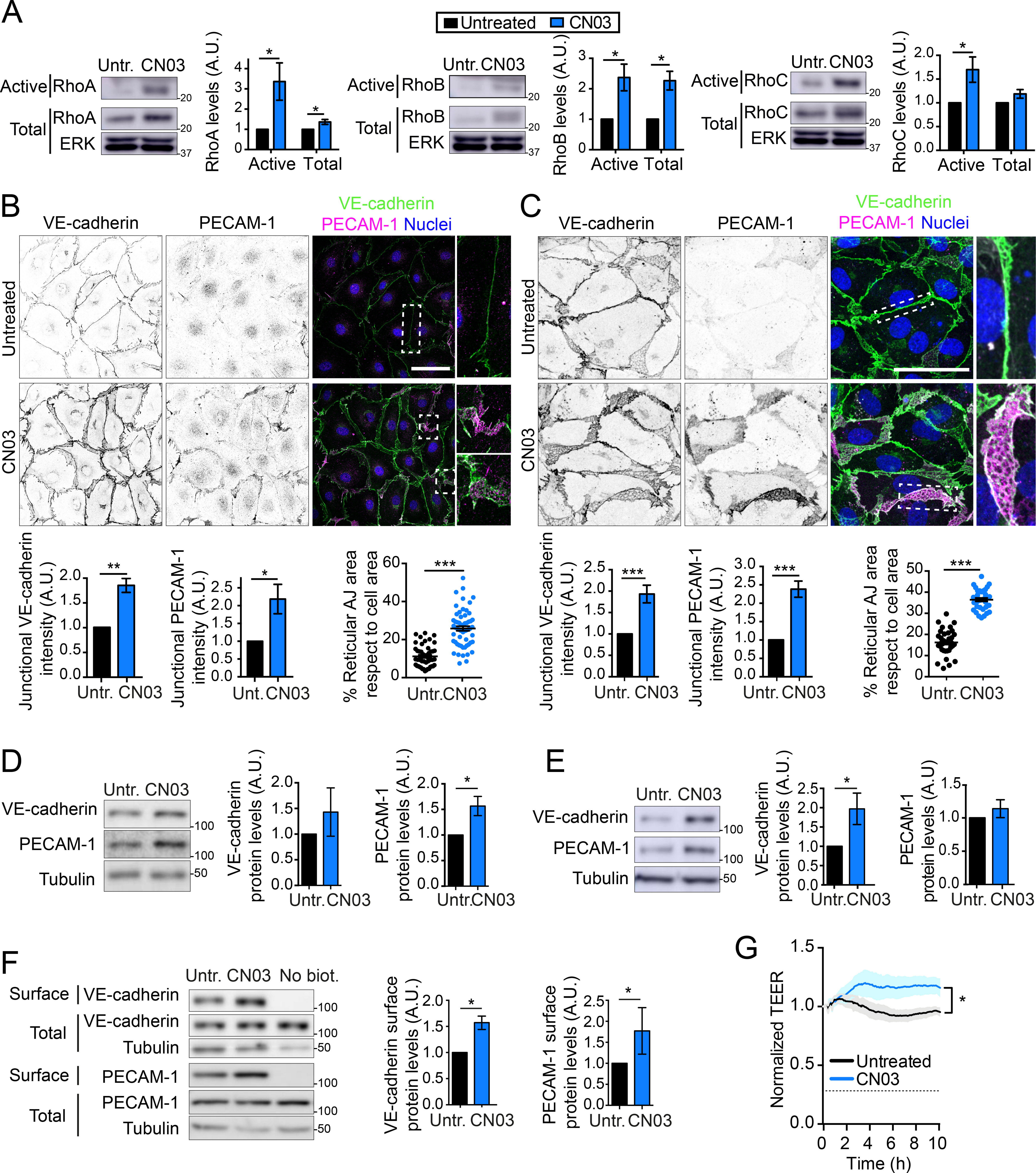
A
Untreated
CN03
Untr.
CN03
Active
RhoA
Total
RhoA
ERK
20
20
37
RhoA levels (A.U.)
0
1
2
3
4
*
*
Active
Total
Untr.
CN03
Active
RhoB
Total
RhoB
ERK
20
20
37
RhoB levels (A.U.)
0
1
2
3
*
*
Active
Total
Untr.
CN03
Active
RhoC
Total
RhoC
ERK
20
20
37
RhoC levels (A.U.)
0.0
0.5
1.0
1.5
2.0
*
Active
Total
B
VE-cadherin
PECAM-1
VE-cadherin
PECAM-1
Nuclei
Untreated
CN03
Junctional VE-cadherin intensity (A.U.)
0.0
0.5
1.0
1.5
2.0
**
Untr.
CN03
Junctional PECAM-1 intensity (A.U.)
0.0
0.5
1.0
1.5
2.0
2.5
*
Unt.
CN03
% Reticular AJ area respect to cell area
0
20
40
60
***
Untr.
CN03
C
VE-cadherin
PECAM-1
VE-cadherin
PECAM-1
Nuclei
Untreated
CN03
Junctional VE-cadherin intensity (A.U.)
0.0
0.5
1.0
1.5
2.0
2.5
***
Untr.
CN03
Junctional PECAM-1 intensity (A.U.)
0.0
0.5
1.0
1.5
2.0
2.5
3.0
***
Untr.
CN03
% Reticular AJ area respect to cell area
0
10
20
30
40
50
***
Untr.
CN03
D
Untr.
CN03
VE-cadherin
PECAM-1
Tubulin
100
100
50
VE-cadherin protein levels (A.U.)
0.0
0.5
1.0
1.5
2.0
Untr.
CN03
PECAM-1 protein levels (A.U.)
0.0
0.5
1.0
1.5
2.0
*
Untr.
CN03
E
Untr.
CN03
VE-cadherin
PECAM-1
Tubulin
100
100
50
VE-cadherin protein levels (A.U.)
0.0
0.5
1.0
1.5
2.0
2.5
*
Untr.
CN03
PECAM-1 protein levels (A.U)
0.0
0.5
1.0
1.5
Untr.
CN03
F
Untr.
CN03
No biot.
Surface
VE-cadherin
Total
VE-cadherin
Tubulin
Surface
PECAM-1
Total
PECAM-1
Tubulin
100
100
50
100
100
50
VE-cadherin surface protein levels (A.U.)
0.0
0.5
1.0
1.5
2.0
*
Untr.
CN03
PECAM-1 surface protein levels (A.U.)
0.0
0.5
1.0
1.5
2.0
2.5
*
Untr.
CN03
G
Normalized TEER
0.0
0.5
1.0
1.5
*
Untreated
CN03
Time (h)
0
2
4
6
8
10

A
VE-cadherin-Dendra2
-0:30
0:00
1:00
2:00
3:00
4:00
5:00
6:00
7:00
8:00 (min)
Untreated
λ = 543 nm
CN03
λ = 543 nm
B
Linear
Reticular
fluorescence % (λ=543 nm)
100
80
60
40
0
2
4
6
8
Time (min)
Untr.
CN03
*
C
fluorescence 543 disappearance rate constant (min⁻¹)
0.05
0.00
-0.05
-0.10
-0.15
*
*
*
*
Linear
Reticular
● Untreated
● CN03
D

A
+LPS
CN03
0h
3h
20h
Normalized TEER
1.2
1.0
0.8
0.6
0.4
0.2
0.0
0
5
10
15
20
LPS
LPS+CN03
Normalized Rb
% TEER decrease (t=10h)
60
40
20
0
*
LPS
LPS+CN03
B
VE-cadherin PECAM-1
F-actin Nuclei
VE-cadherin
PECAM-1
Intercellular gaps
Untreated
LPS
LPS + CN03
Untreated
LPS
LPS+CN03
Junctional VE-cad. intensity (A.U.)
1.5
1.0
0.5
0.0
*
Junctional PECAM-1 intensity (A.U.)
***
*
% Area with intercellular gaps
15
10
5
0
C
Normalized TEER
1.5
1.0
0.5
0.0
*
FBS
Healthy
Sepsis
D
VE-cadherin PECAM-1
F-actin Nuclei
VE-cadherin
PECAM-1
Intercellular gaps
Untreated
Sepsis
Sepsis + CN03
E
% Area with intercellular gaps
100
80
60
40
20
0
***
***
***
Untreated
Sepsis
Sepsis +CN03

A
Saline
CN03
LPS
VEGF
Saline
LPS
VEGF
Saline
Fold-change
Evans Blue extravasation
(O.D.595nm/mg tissue)
LPS
0
2
4
6
*
Saline
CN03
VEGF
0
1
2
3
4
p=0.055
Saline
CN03
B
ΔIL-6
plasma concentration (pg/ml)
0
1000
2000
3000
4000
**
***
*
p=0.06
Saline
LPS
LPS+CN03
LPS+CN03(x3)
ΔTNF
plasma concentrartion (pg/ml)
0
50
100
150
200
250
***
**
**
*
*
Saline
LPS
LPS+CN03
LPS+CN03(x3)
C
Liver
Vascular leakage
(O.D.595nm)
0.0
0.1
0.2
0.3
0.4
*
***
***
*
Saline
LPS
LPS+CN03
LPS+CN03(x3)
Lung
0.0
0.1
0.2
0.3
0.4
**
p=0.065
*
Saline
LPS
LPS+CN03
LPS+CN03(x3)
Kidney
0.0
0.1
0.2
0.3
0.4
*
**
***
*
***
Saline
LPS
LPS+CN03
LPS+CN03(x3)

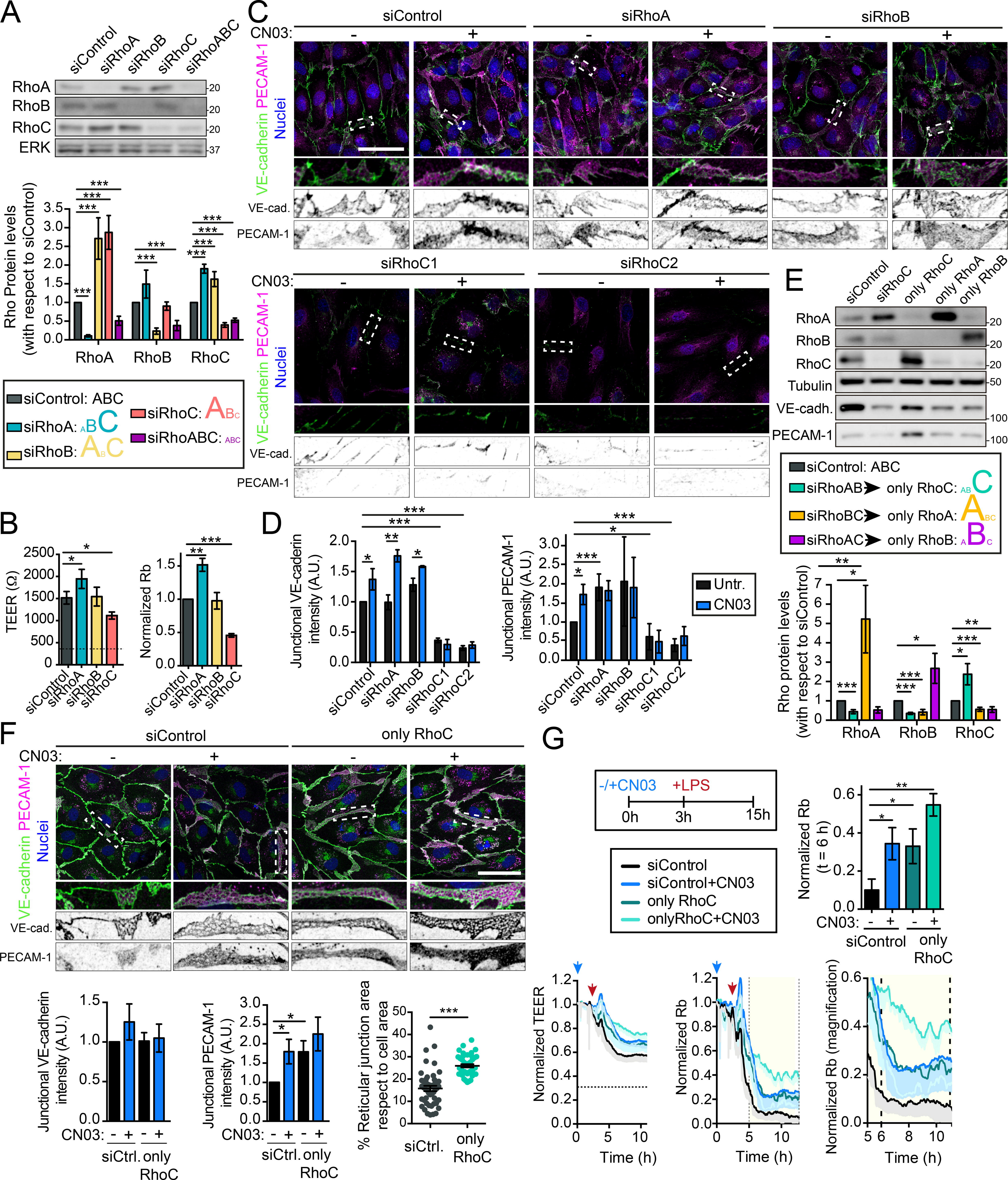
A
siControl
siRhoA
siRhoB
siRhoC
siRhoABC
RhoA
RhoB
RhoC
ERK
-20
-20
-20
-37
Rho Protein levels (with respect to siControl)
3.5
3.0
2.5
2.0
1.5
1.0
0.5
0.0
***
RhoA
RhoB
RhoC
siControl: ABC
siRhoA: ABC
siRhoB: ABC
siRhoC: ABC
siRhoABC: ABC
B
TEER (Ω)
2500
2000
1500
1000
500
0
*
Normalized Rb
1.5
1.0
0.5
0.0
**
***
siControl
siRhoA
siRhoB
siRhoC
C
siControl
siRhoA
siRhoB
CN03:
-
+
VE-cadherin PECAM-1 Nuclei
VE-cad.
PECAM-1
siRhoC1
siRhoC2
D
Junctional VE-caderin intensity (A.U.)
2.0
1.5
1.0
0.5
0.0
Junctional PECAM-1 intensity (A.U.)
3.0
2.5
2.0
1.5
1.0
0.5
0.0
Untr.
CN03
siControl
siRhoA
siRhoB
siRhoC1
siRhoC2
E
siControl
siRhoC
only RhoC
only RhoA
only RhoB
RhoA
RhoB
RhoC
Tubulin
VE-cadh.
PECAM-1
-20
-20
-20
-50
-100
-100
siControl: ABC
siRhoAB ➤ only RhoC: ABC
siRhoBC ➤ only RhoA: ABC
siRhoAC ➤ only RhoB: ABC
Rho protein levels (with respect to siControl)
7
6
5
4
3
2
1
0
RhoA
RhoB
RhoC
F
siControl
only RhoC
CN03:
-
+
VE-cadherin PECAM-1 Nuclei
VE-cad.
PECAM-1
Junctional VE-cadherin intensity (A.U.)
1.5
1.0
0.5
0.0
Junctional PECAM-1 intensity (A.U.)
3.0
2.5
2.0
1.5
1.0
0.5
0.0
CN03:
siCtrl.
only RhoC
% Reticular junction area respect to cell area
50
40
30
20
10
0
***
siCtrl.
only RhoC
G
-/+CN03
+LPS
0h
3h
15h
siControl
siControl+CN03
only RhoC
onlyRhoC+CN03
Normalized Rb (t = 6 h)
0.6
0.4
0.2
0.0
**
*
*
CN03:
siControl
only RhoC
Normalized TEER
1.2
1.0
0.8
0.6
0.4
0.2
0.0
Time (h)
0
5
10
Normalized Rb
Normalized Rb (magnification)
0.6
0.4
0.2
0
5
6
8
10

A
Label Free
Quantitative proteomics
Control
siRhoC1
siRhoC2
RhoC
-Log10 p-value
Log10 Abundance Ratio
(siRhoC1 / siControl)
(siRhoC2 / siControl)
B
(x10^6)
Normalized abundance
MYL9 (MLC)
(x10^9)
Normalized Abundance
MYL6
(x10^6)
MYL6B
(x10^8)
MYL12B
C
siControl
siRhoA
siRhoB
siRhoC
siRhoA+B+C
ERK
RhoA
RhoB
RhoC
P-MYL9 (MLC)
MYL9(MLC)
Normalized total MLC levels
siRhoABC
D
siControl
siRhoA
siRhoB
siRhoC
F-actin
p-MLC
VE-cadherin p-MLC F-actin Nuclei
Fluorescence intensity
Distance (μm)
E
Normalized total F-actin intensity
% F-actin (periphery)
Normalized total p-MLC intensity
% p-MLC (periphery)
F
siControl
only RhoC
VE-cadherin PECAM-1 F-actin Nuclei
F-actin
Normalized total F-actin intensity
% F-actin (periphery)
Fluorescence intensity
Distance (μm)
G
Untreated
CN03
VE-cadherin PECAM-1 F-actin Nuclei
F-actin
Normalized total F-actin intensity
Untr.
CN03
% F-actin (periphery)
Fluorescence intensity
Distance (μm)
***

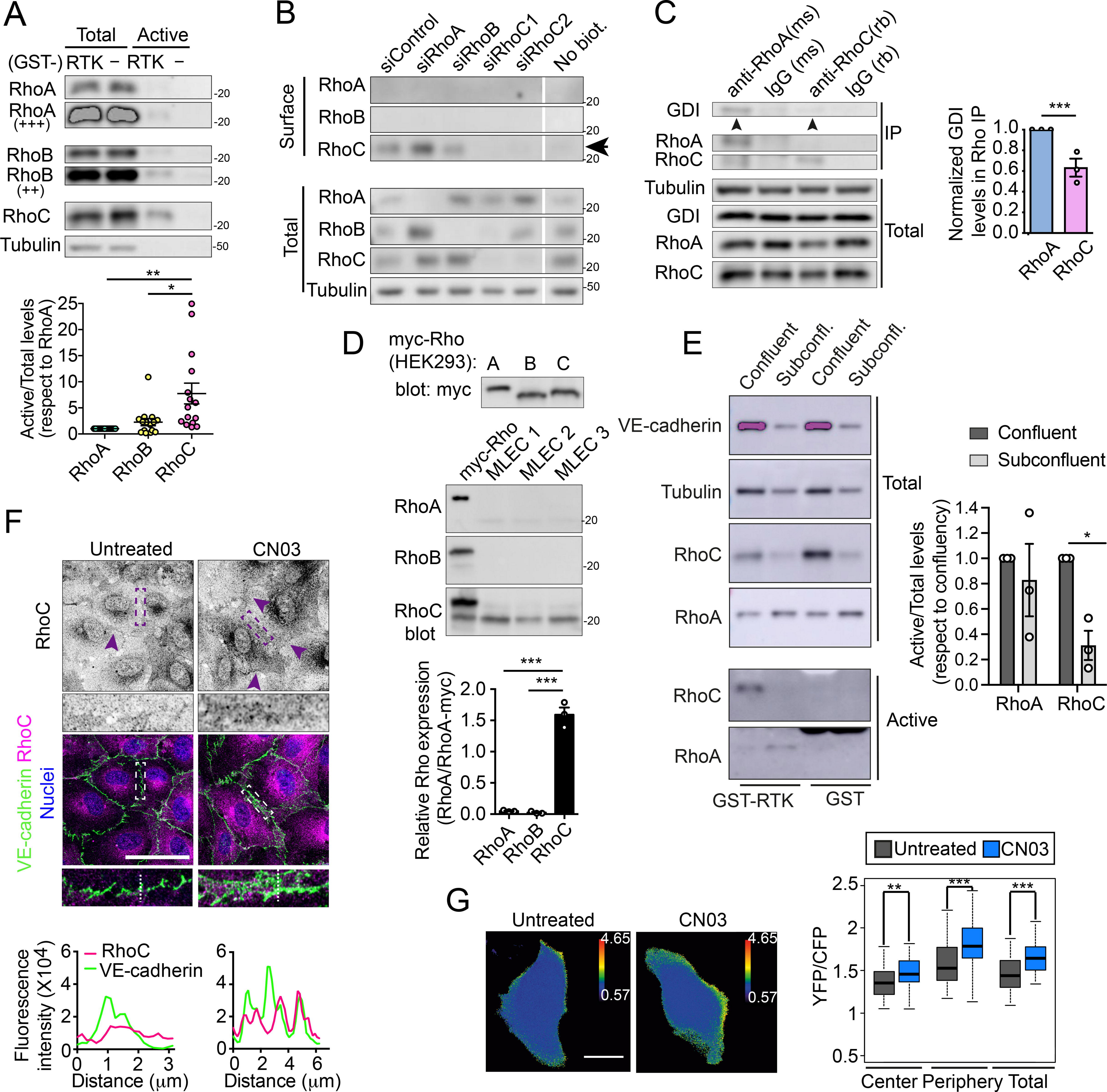
A
Total
Active
(GST-) RTK – RTK –
RhoA
RhoA (+++)
RhoB
RhoB (++)
RhoC
Tubulin
-20
-50
**
*
Active/Total levels (respect to RhoA)
0
5
10
15
20
25
RhoA
RhoB
RhoC
B
siControl
siRhoA
siRhoB
siRhoC1
siRhoC2
No biot.
Surface
Total
RhoA
RhoB
RhoC
Tubulin
-20
-50
C
anti-RhoA(ms)
IgG (ms)
anti-RhoC(rb)
IgG (rb)
GDI
RhoA
RhoC
IP
Tubulin
GDI
RhoA
RhoC
Total
***
Normalized GDI levels in Rho IP
0.0
0.2
0.4
0.6
0.8
1.0
RhoA
RhoC
D
myc-Rho (HEK293): A B C
blot: myc
myc-Rho
MLEC 1
MLEC 2
MLEC 3
RhoA
RhoB
RhoC blot
-20
***
***
Relative Rho expression (RhoA/RhoA-myc)
0.0
0.5
1.0
1.5
2.0
RhoA
RhoB
RhoC
E
Confluent
Subconfl.
Confluent
Subconfl.
VE-cadherin
Tubulin
RhoC
RhoA
Total
RhoC
RhoA
Active
GST-RTK
GST
Confluent
Subconfluent
*
Active/Total levels (respect to confluency)
0.0
0.2
0.4
0.6
0.8
1.0
1.2
1.4
RhoA
RhoC
F
Untreated
CN03
RhoC
VE-cadherin RhoC Nuclei
RhoC
VE-cadherin
Fluorescence intensity (X104)
0
2
4
6
Distance (μm)
0 1 2 3
0 2 4 6
G
Untreated
CN03
4.65
0.57
Untreated
CN03
**
***
***
YFP/CFP
0.5
1
1.5
2
2.5
Center
Periphery
Total

A
Prenylation
190
GFP
GGGARRGKKKSGCLVL RhoA-hyper
GFP
GGGVRKNKRRRGCPIL RhoC-hyper
188
Hypervariable region
Manders´ coefficient (GFP-Rho-hyper /peripheral VE-cad.)
1.0
0.8
0.6
0.4
0.2
0.0
***
***
***
***
***
GFP-RhoA-hyper
GFP-RhoA-hyperS188R
GFP-RhoA-hyper C190G
GFP-RhoC-hyper
GFP-RhoC-hyper R188S
GFP-RhoC-hyper C190G
GFP-Rho hipervariable region VE-cadherin
GFP-RhoA-hyper
GFP-RhoA-hyperS188R
GFP-RhoA-hyperC190G
GFP-RhoC-hyper
GFP-RhoC-hyperR188S
GFP-RhoC-hyperC190G
B
GFP-Rho VE-cad.
GFP-RhoA
GFP-RhoC
GFP-RhoCR188S
GFP-RhoCR188A
Manders´ coefficient (GFP-Rho/peripheral VE-cad.)
0.6
0.5
0.4
0.3
0.2
0.1
0.0
***
***
***
GFP-RhoA
GFP-RhoC
GFP-RhoC(R188S)
GFP-RhoC(R188A)
C
GFP
GFP-RhoA
GFP-RhoC
GFP-RhoCR188S
GFP-RhoCR188A
GFP
GFP-RhoA
GFP-RhoC
GFP-RhoCR188S
GFP-RhoCR188A
RhoA (GFP)
RhoA
RhoC (GFP)
RhoC
GFP
GFP (+++)
GAPDH
blot
-50
-25
-50
-25
-50
-50
-37
-37
MW
Total
Active
Normalized Active/Total levels (respect to GFP-RhoC)
1.0
0.8
0.6
0.4
0.2
0.0
***
***
***
GFP-RhoA
GFP-RhoC
GFP-RhoCR188S
GFP-RhoCR188A
D
GFP
GFP-RhoA
GFP-RhoC
GFP-RhoCR188S
Normalized Rb
1.4
1.2
1.0
0.8
0.6
0.4
0.2
0.0
*
**
0
5
10
15
20
Time (h)